Rings and Things

David Ormrod Morley

Balliol College

University of Oxford

A thesis submitted for the degree of

Doctor of Philosophy

Trinity 2020

Contents

List of Notes By David

List of Notes By Mark

1 | Computational Methods

The theoretical basis of Monte Carlo methods and their application to generating realisations of two-dimensional networks is reviewed. There is a broad discussion of Metropolis Monte Carlo methods, before specific methods are covered in detail; namely the bond switching algorithm and hard particle Monte Carlo in conjunction with the Voronoi construction. This discussion lays the groundwork for the extension of these methods and development of additional Monte Carlo algorithms in subsequent chapters.

1.1 General Monte Carlo Methods

Monte Carlo methods are a class of computational algorithms designed to solve complex problems stochastically. These normally fall into the broad categories of calculating integrals, sampling probability distributions and finding global minima of very high dimensional functions - tasks which are often incredibly hard to compute deterministically. Since their initial development in the mid-20$^{\text{th}}$ century, such methods have become an invaluable tool for solving problems in the physical sciences. Monte Carlo methods are used in this context for calculating thermodynamic averages of properties in equilibrium systems; finding the minima in potential energy surfaces of small molecules, glasses, crystals and biomolecules; as well as non-equilibrium simulations such as growth of crystals and thin-films [71–76]. In this thesis these Monte Carlo methods will be used in a variety of contexts: chapter **??** simulates the growth of bilayer materials using a random sequential growth algorithm; chapter **??** optimises a cost function to control network structure; chapter **??** samples amorphous configurations of various system topologies; chapter

2 samples the phase space of hard particle assemblies and chapter **??** finds solutions to the procrystalline problem, essentially via global optimisation. Therefore, the general theory is presented here with specific details of two established methods: bond switching and hard particle Monte Carlo given in the following section.

1.1.1 Statistical Mechanics

The total energy of a system with a fixed number of particles, $\mathcal{N}$, is given by the Hamiltonian,

$$\mathcal{H}(\mathbf{p},\mathbf{r}) = \mathcal{K}(\mathbf{p}) + \mathcal{U}(\mathbf{r}) \,, \tag{1.1}$$

where $\mathcal{K}(\mathbf{p})$ is the kinetic energy as a function of all particle momenta and $\mathcal{U}(\mathbf{r})$ is the potential energy as a function of all particle positions [77]. The positions and momenta comprise the phase space of the system. At fixed volume, $\mathcal{V}$, and temperature, T, all the the essential thermodynamic information is then provided through the classical canonical partition function:

$$Q = \frac{1}{h^{D\mathcal{N}}\mathcal{N}!} \int \mathrm{d}\mathbf{p}\,\mathrm{d}\mathbf{r}\, \exp\left[-\mathcal{H}(\mathbf{p},\mathbf{r})/k_\mathrm{B}T\right], \tag{1.2}$$

where D is the number of spatial dimensions. This can be factorised into kinetic and potential components as

$$Q = \frac{1}{h^{D\mathcal{N}}\mathcal{N}!} \int \mathrm{d}\mathbf{p}\, \exp\left[-\mathcal{K}(\mathbf{p})/k_\mathrm{B}T\right] \int \mathrm{d}\mathbf{r}\, \exp\left[-\mathcal{U}(\mathbf{r})/k_\mathrm{B}T\right], \tag{1.3}$$

where

$$Z = \int \mathrm{d}\mathbf{r}\, \exp\left[-\mathcal{U}(\mathbf{r})/k_\mathrm{B}T\right] \tag{1.4}$$

is the configurational integral [78]. As will be shown, in Monte Carlo simulations it is the energetic differences between configurations that are required, and so at constant temperature the kinetic component can be neglected and it is only the configurational integral that is of importance. In this case the probability density of the system being in the configuration $\mathbf{r}$ is given by the Boltzmann distribution:

$$P(\mathbf{r}) = \frac{\exp\left[-\mathcal{U}(\mathbf{r})/k_\mathrm{B}T\right]}{Z} \,. \tag{1.5}$$

This allows the expectation value of an observable of the system, $\mathcal{A}(\mathbf{r})$, to be determined from:

$$\langle A \rangle = \int \mathrm{d}\mathbf{r}\, \mathcal{A}(\mathbf{r})\, P(\mathbf{r}) \ . \tag{1.6}$$

The expectation value is then the ratio of two $\mathcal{N}D$ dimensional integrals. The next section shows how these can be evaluated by Monte Carlo sampling.

1.1.2 Importance Sampling

An integral of form (1.6) can be evaluated numerically by a number of methods. As an illustration, consider the simple example of a two-dimensional potential energy surface in figure 1.1. To calculate the expectation value of the potential energy one must evaluate the integral

$$\langle \mathcal{U} \rangle = \int_0^{L_y} \int_0^{L_x} \mathrm{d}x\mathrm{d}y\, \mathcal{U}(x,y)\, \mathcal{P}(x,y) \ . \tag{1.7}$$

One way to achieve this would be to use standard numerical methods such as the trapezium rule or Simpson's rule to calculate the potential energy over a regular grid of points, as in figure 1.1a, weighting each according to the Boltzmann distribution.

An alternative would be to take a stochastic approach. In the simplest implementation, a series of S random sampling points, (x_i, y_i), can be generated uniformly in the intervals $[0, L_x]$ and $[0, L_y]$, as in figure 1.1b. Weighting these according to the Boltzmann distribution and averaging gives an estimation to the integral:

$$\langle \mathcal{U} \rangle = \frac{L_x L_y}{S} \sum_{i=1}^{S} \mathcal{U}(x_i, y_i)\, \mathcal{P}(x_i, y_i) \ , \tag{1.8}$$

which converges to the exact value as $S \to \infty$.

However, both quadrature and Monte Carlo uniform sampling suffer from the same inefficiency. As can be seen in both schemes, many of the sampling points fall in regions of phase space where the potential energy is high and hence the weighting probability distribution is very small at reasonable temperatures. In effect, significant effort is spent calculating regions where the contribution to the total integral is negligible. A better approach is therefore to generate a series of S random

sampling points, (x_i, y_i), according to the distribution $\mathcal{P}(x, y)$, as in figure 1.1b. The expectation value of the observable can then be calculated using a simple average:

$$\langle \mathcal{U} \rangle = \frac{1}{S} \sum_{i=1}^{S} \mathcal{U}(x_i, y_i) \ . \tag{1.9}$$

This is known as importance sampling and is vastly more efficient when dealing with an aggressive probability distribution like the Boltzmann, where only a small proportion of the phase space is accessible.

Whilst this scheme is ideal theoretically, it is impracticable for physical systems. This is because for any problem of real interest one lives in a "black box" where the functional form of the potential energy surface in its hundreds if not thousands of dimensions is unknown. In this case often the only way of learning about the form is by on-the-fly exploration of the surface [79]. This can be achieved by talking a random walk through configurational space using Markov chain Monte Carlo.

1.1.3 Markov Chain Monte Carlo

Markov chain Monte Carlo provides a framework to perform importance sampling on a potential energy surface. A system of interest can exist in a (very large) number of configurational states, $\{\mathbf{r}_0, \mathbf{r}_1, \ldots, \mathbf{r}_M\}$. A Markov chain can then be constructed from this set, whereby a sequence of states is generated stochastically across a series of steps, $s = 0, 1, \ldots, S$. In this process, the probability of moving between states at each step is given by the transition matrix, $\boldsymbol{\pi}$, where each element, π_{ij}, gives the probability of moving from the state $\mathbf{r}_i$ to another state $\mathbf{r}_j$. This leads to the two relationships:

$$0 \leq \pi_{ij} \leq 1 \,, \tag{1.10}$$

$$\sum_j \pi_{ij} = 1 \,, \tag{1.11}$$

the first being a statement of the probabilistic nature of the elements whilst the second ensures all transfer remains within the state space [77–79].

The probability that the system is in each state at a given step, s, can be represented by the row vector $\mathbf{P}_s$. This probability distribution evolves with each

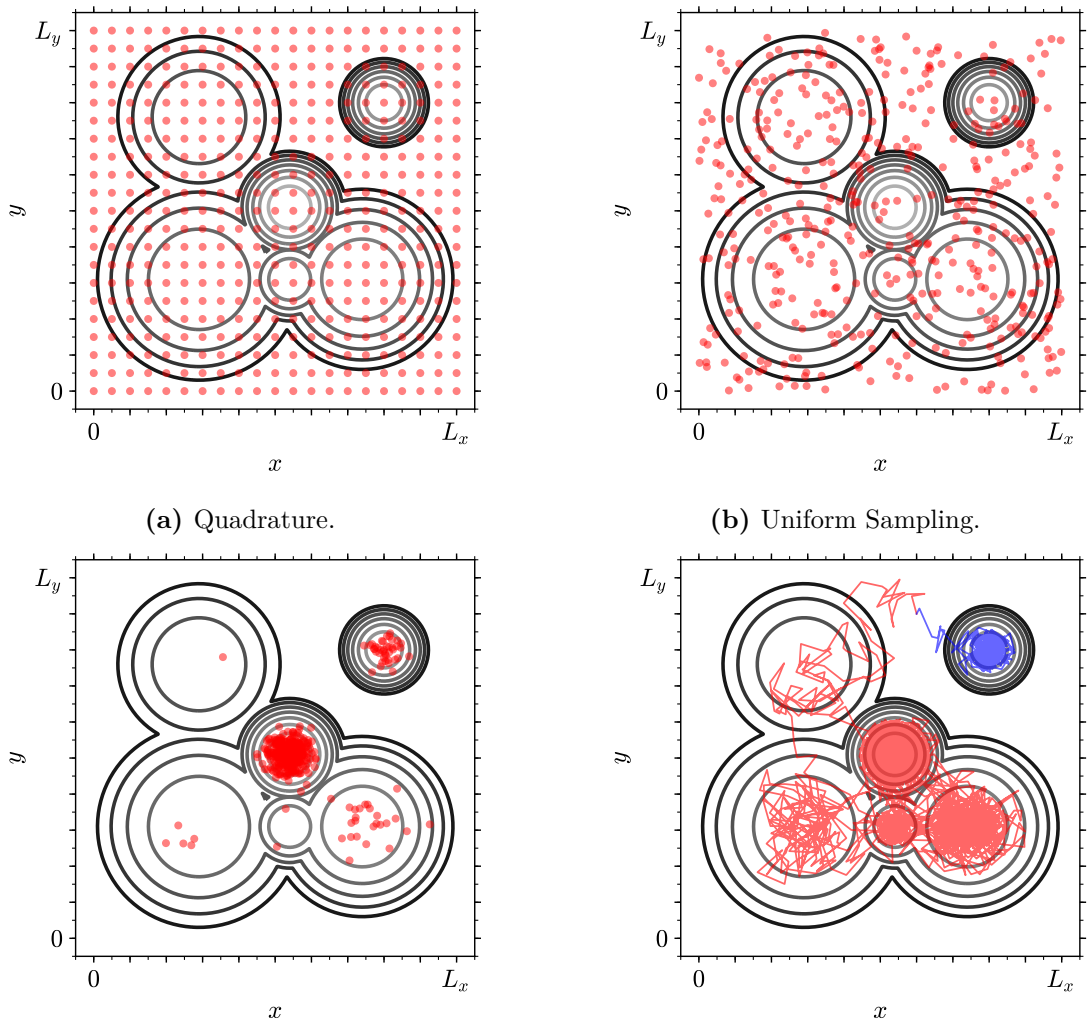

(a) Quadrature.

(b) Uniform Sampling.

(c) Importance Sampling.

(d) Markov Chain Monte Carlo

Figure 1.1: Demonstration of different sampling methods with an example two-dimensional potential energy surface (contour lines). Panels(a)-(c) display the same number of (red) sampling points. Panel (a) shows conventional quadrature where the surface is divided into a regular grid of sampling points which are then weighted by the Boltzmann distribution. Panel (b) shows Monte Carlo sampling with a uniform distribution of points which again must be Boltzmann-weighted. Panel (c) shows Monte Carlo importance sampling with points now selected according to the Boltzmann distribution. Panel (d) shows Markov chain Monte Carlo with two random walks through phase space (red and blue lines) starting from different random seeds.

step as $\mathbf{P}_{s+1} = \mathbf{P}_s\boldsymbol{\pi}$, so that starting from any initial distribution, $\mathbf{P}_0$, it follows that $\mathbf{P}_S = \mathbf{P}_0\boldsymbol{\pi}^S$. The question is then as to the behaviour as $S \to \infty$. Provided certain criteria are met, the distribution will tend to a stationary distribution,

$\mathbf{P}$, which satisfies the eigenvalue equation

$$\mathbf{P} = \mathbf{P}\boldsymbol{\pi} \,, \tag{1.12}$$

regardless of the initial distribution (although the speed of the convergence does depend on $\mathbf{P}_0$). This will occur only if the system is *ergodic*, meaning that every state is connected to every other by some finite path.

In a discrete analogue to equation (1.6), the expectation value of an observable, A, can be calculated from the ensemble average:

$$\langle A \rangle = \sum_{i=1}^{M} A\left(\mathbf{r}_i\right) \mathcal{P}\left(\mathbf{r}_i\right) \,, \tag{1.13}$$

where $\mathcal{P}\left(\mathbf{r}_i\right)$ are the elements of $\mathbf{P}$. However, as previously mentioned the number of discrete states is usually exceedingly large and so calculating the average over all states is not possible. The solution is to take a random walk across through configurational space, sampling explicit states to form the chain $X_0, X_1, \ldots, X_S$; where each move is chosen randomly according to the transition matrix $\boldsymbol{\pi}$. In this case the expectation of the same observable can be calculated from the average over the sampled states:

$$\langle A \rangle = \frac{1}{S} \sum_{i=1}^{S} A\left(X_i\right) \,, \tag{1.14}$$

where the true value is approached as $S \to \infty$.

In this section the problem of sampling phase space efficiently has been reformulated, but as yet not solved. This is because the form of the transition matrix is still unknown. Instead only the ideal form of the limiting probability distribution, $\mathbf{P}$, is available - where the elements follow the Boltzmann probabilities in equation (1.5). A practical solution to this problem is provided by the Metropolis algorithm.

1.1.4 Metropolis Algorithm

The Metropolis algorithm gives a prescription of how to construct a transition matrix, $\boldsymbol{\pi}$, with the requisite properties that samples the Boltzmann distribution

[80]. Firstly, combining equations (1.11) and (1.12) gives a condition on the transition matrix known as global balance:

$$\sum_j \mathcal{P}(\mathbf{r}_i)\,\pi_{ij} = \sum_j \mathcal{P}(\mathbf{r}_j)\,\pi_{ji}\,. \tag{1.15}$$

Whilst it is possible to construct transition matrices which satisfy only global balance [81–83], it is practically simpler to satisfy global balance by applying the stronger condition of detailed balance:

$$\mathcal{P}(\mathbf{r}_i)\,\pi_{ij} = \mathcal{P}(\mathbf{r}_j)\,\pi_{ji}\,. \tag{1.16}$$

In the Metropolis algorithm the off-diagonal elements of the transition matrix are written as the product of two probabilities:

$$\pi_{ij} = \begin{cases} \tau_{ij}P_{ij} & i \neq j \\ 1 - \sum\limits_{j\neq i} \tau_{ij}P_{ij} & i = j \end{cases}, \tag{1.17}$$

where τ_{ij} is the trial probability of moving from state $\mathbf{r}_i$ to $\mathbf{r}_j$ and P_{ij} is the probability of accepting the trial move. To conform to detailed balance, the trial probabilities must be chosen to satisfy $\tau_{ij} = \tau_{ji}$. Then, in the crux of the algorithm, the acceptance probabilities are given by

$$P_{ij} = \begin{cases} 1 & \mathcal{P}(\mathbf{r}_j) \geq \mathcal{P}(\mathbf{r}_i) \\ \frac{\mathcal{P}(\mathbf{r}_j)}{\mathcal{P}(\mathbf{r}_i)} & \mathcal{P}(\mathbf{r}_j) < \mathcal{P}(\mathbf{r}_i) \end{cases} = \begin{cases} 1 & \mathcal{U}(\mathbf{r}_j) \leq \mathcal{U}(\mathbf{r}_i) \\ \frac{\exp[-\mathcal{U}(\mathbf{r}_j)/k_\mathrm{B}T]}{\exp[-\mathcal{U}(\mathbf{r}_i)/k_\mathrm{B}T]} & \mathcal{U}(\mathbf{r}_j) > \mathcal{U}(\mathbf{r}_i) \end{cases}, \tag{1.18}$$

which can be expressed more succinctly as

$$P_{ij} = \min\Big[1, \exp\left[-\Delta\mathcal{U}/k_\mathrm{B}T\right]\Big], \tag{1.19}$$

where $\Delta\mathcal{U}$ is the difference in potential energy between the final and initial states. The elegance of the Metropolis algorithm lies in the fact that the acceptance probability depends only on the ratio of the configuration probabilities removing the need for a normalising factor. This means the relative probabilities can be used (which are computable) instead of the absolute probabilities (which are unknowable).

The final stage is the choice of the matrix of trial probabilities, $\boldsymbol{\tau}$. This is very flexible and one can be creative in the selection of trial moves, providing

that the underlying matrix is symmetric and ergodic. An effective strategy is to choose moves in which the trial state is relatively close to the current state to trace the paths of high probability in the system. A summary of the Metropolis algorithm is therefore as follows:

1. Initialise the system in a state $X_{s=0}$ and calculate the potential energy $\mathcal{U}(X_s)$
2. Generate a trial state X_t (a perturbation of X_s) according to τ_{st}
3. Calculate the potential energy of the trial state $\mathcal{U}(X_t)$
4. Determine acceptance or rejection of the trial move according to the Metropolis criterion (1.19)
5. Update the system to the new state: if the trial move is accepted $X_{s+1} = X_t$ otherwise $X_{s+1} = X_s$
6. Repeat steps 2-5

There are a few practical factors related to the scheme above. In Markov chain Monte Carlo it was previously mentioned that it takes time for the system to evolve to the stationary distribution. Therefore it is necessary to have an equilibration period where the chain is generated but not used for sampling of observables. In addition, whilst selecting trial moves close to the current state increases efficiency, it introduces correlation into the procedure. A way around this is to not calculate observables based on every step, but rather after a number of statistically significant steps.

As an example of the Metropolis algorithm, consider again the two-dimensional potential energy surface in figure 1.1d. Here two simulation paths are displayed in red and blue, starting from the same initial state but with different starting points in the random number generators *i.e.* random seeds. As can be seen the Metropolis algorithm takes a random walk over the configurational space, conducting importance sampling as in 1.1c. However, in this example highlights a potential problem. There are two regions of phase space with non-zero probabilities which are separated by a relatively large energy barrier. Although they are in principle linked

by a path, the barrier may effectively mean they are disconnected on a reasonable simulation time scale, breaking ergodicity. This manifests as the red walk sampling one region and the blue walk being trapped in the other region. Using multiple seeds in this way helps to identify if any such behaviour is present. If it leads to significant differences in the computed averages, more advanced techniques using enhanced sampling may have to be employed [84, 85].

1.1.5 Global Optimisation & Simulated Annealing

So far in this section it has been shown how Monte Carlo methods can be used perform importance sampling of potential energy surfaces. These methods can also be used to solve the related problem of finding global minima in potential energy surfaces and other more general functions. Consider the case where there is an objective function, $\Omega(\mathbf{r})$, which depends on particle positions. If it is known that there exists a solution where $\Omega(\mathbf{r}) = 0$, it may be sufficient to perform a standard random walk of the type in figure 1.1d until a solution is found, using the more general Metropolis criterion:

$$P_{ij} = \min\left[1, \exp\left[-\Delta\Omega/k_{\mathrm{B}}T\right]\right]. \tag{1.20}$$

There is of course a chance that the optimisation will not converge to the global minimum, most likely getting trapped in a local minimum (as for instance the blue path in 1.1d). One solution to this problem is just to keep restarting the algorithm with different initial conditions until the global minimum is obtained.

Often however the value of the global minimum is not known, as is the case for a potential energy surface, and this rudimentary approach is insufficient. One must then employ a more sophisticated technique to find the global minimum of a very high dimensional and potentially rough surface. This in itself is an extensive area of study and there are many approaches such as using genetic algorithms or basin-hopping [86–88]. This thesis will use simulated annealing, which can be considered an extension to Metropolis Monte Carlo [89]. In addition simulated annealing is effective for searching surfaces with many similar minima as in glasses - the name reflecting its origins in the analogous process in metallurgy to generate defect free metals.

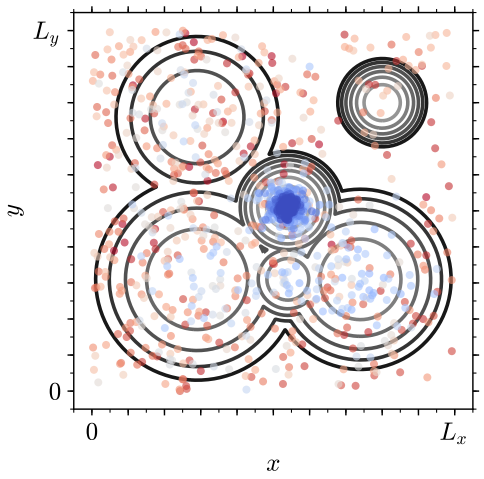

Figure 1.2: Demonstration of the simulated annealing algorithm on a two-dimensional potential energy surface, with states coloured by temperature (red→blue indicating hot→cold. As the temperature is reduced the state converges on the global minimum.

The simulated annealing algorithm proceeds as follows. The system of interest is first thermalised by performing Metropolis Monte Carlo at infinite temperature *i.e.* accepting every move. The system is then gradually cooled to zero temperature, with the Metropolis criterion (1.20) reducing the proportion of accepted moves. In theory if the cooling is infinitely slow, the system is maintained in thermal equilibrium and will eventually reach the global minimum [90]. In practice this is not realisable and so a cooling rate must be empirically selected. Still it is possible for trapping to occur in local minima, especially if the transition between low energy states is very slow. As before, one can then cycle the simulated annealing, repeatedly heating and cooling the system until the global minimum is found. The simulated annealing algorithm is demonstrated with the two-dimensional potential energy surface in figure 1.2. As can be seen at high temperature the entire surface is sampled, overcoming all energy barriers, but as cooling takes place the system settles into the low energy regions of the surface, finally terminating in the global minimum.

1.2 Bond Switching Monte Carlo

Bond switching Monte Carlo was originally developed by Wooten, Winer and Weaire to generate high quality configurations of three dimensional silica glass

[91]. The basic principle is to amorphise a crystalline lattice with a series of transformations that swap the nearest neighbours of pairs of atoms and optimise the resulting structure to generate a continuous random network which is well-relaxed. These continuous random network models replicate experimental observables with high accuracy (including bond length and angle distributions, radial distribution functions, electronic band gaps and Raman spectra) and have since been applied to alternative systems such as three-dimensional amorphous carbon, binary glasses and biological polymers [92–97]. However, the method can also be readily modified to study two-dimensional systems, as has been done for amorphous graphene and silica, and which forms the basis for much of the work in this thesis, particularly in chapters **??** and **??** [29, 98]. The basic algorithmic details are described in this section, with extensions given in sections again ref later .

1.2.1 Algorithmic Details

The two-dimensional bond switching algorithm essentially follows the prescription of simulated annealing in section 1.1.5. A skeleton algorithm structure is outlined below, followed by specific details [99]. Visualisations are provided for reference in figure 1.3.

1. Generate initial crystalline hexagonal lattice
2. Thermalise the lattice with a large number of random moves
3. Sample configurations by annealling the system slowly at finite temperature, accepting moves according to the Metropolis criterion 1.19

The Monte Carlo move for 3-coordinate atomic materials is essentially the introduction of a Stone-Wales defect into the lattice, which augments the size of two rings and decrements two others, preserving both the mean ring size and the coordination number of the individual atoms involved in the transformation [14]. As defects become more concentrated they overlap, leading to increasing diversity into the ring structure (allowing access to more than the pentagons and heptagons in a single Stone-Wales defect). Each bond transposition is followed by

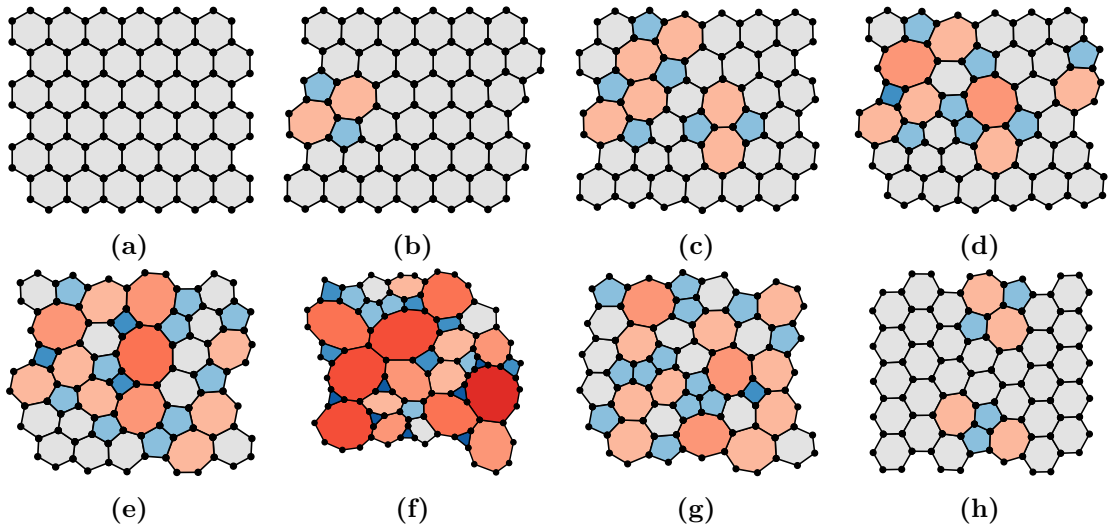

Figure 1.3: Configurations taken from stages of the two-dimensional bond switching algorithm. A crystalline lattice (a) is first thermalised to generate a random high energy network (f) by sequential overlapping Stone-Wales defects (b)-(e). Sampling then occurs as the system is slowly annealed (g)-(h), allowing access to defect states that are not initially obtainable from the crystal structure.

geometry optimisation to minimise and calculate the total energy of the system. A key aspect in the bond switching algorithm is therefore the choice of potential model. The potential models and geometry optimisation process used in this thesis can be found in subsections below.

Cooling the system slowly ensures that the material remains in thermodynamic equilibrium, allowing configurations to be sampled throughout the simulation. The ring structure of the system is then related to the temperature parameter, with more extreme ring sizes appearing at higher temperatures (compare figure 1.3f-1.3h). This simply reflects the inherent balance of enthalpic *vs.* entropic considerations. Figure 1.3h also demonstrates the importance of cooling a randomised lattice instead of heating a crystal, as some low energy defects may have a multi-step formation with a high energy barrier.

1.2.2 Potential Models

The nature of the bond switching method lends itself to the use of semi-empirical potentials which have explicit stretching and angular neighbour lists. As such a popular choice for materials modelling is the Keating potential and modifications

thereof [100, 101]. For a two-dimensional system the Keating potential has the form:

$$\mathcal{U}(\mathbf{r}) = \frac{3}{16}\frac{K_S}{r_0^2} \sum_{\substack{i,j\in \\ \text{stretches}}} \left(r_{ij}^2 - r_0^2\right)^2 + \frac{3}{8}\frac{K_A}{r_0^2} \sum_{\substack{ijk\in \\ \text{angles}}} \left(r_{ij}r_{ik}\cos\theta_{ijk} - r_0^2\cos\theta_0\right)^2 , \quad (1.21)$$

where r_{ij} the distance and θ_{ijk} the angle between particles; whilst K_S and K_A are the force constants for the stretching and angular terms respectively [99]. This potential drives the system towards equilibrium values of r_0 for the bond lengths and θ_0 for the bond angles. The Keating potential has been parametrised for a range of specific materials [99, 102].

However, a more generic potential model is sometimes required which captures the same essential physics. This is provided through the simplified Keating potential [103],

$$\mathcal{U}(\mathbf{r}) = \frac{K_S}{2} \sum_{\substack{i,j\in \\ \text{stretches}}} \left(r_{ij} - r_0\right)^2 + \frac{K_A}{2} \sum_{\substack{i,j,k\in \\ \text{angles}}} \left(\cos\theta_{ijk} - \cos\theta_0\right)^2 , \quad (1.22)$$

which is harmonic in stretching and angular terms. One final modification can be made to this potential. Sometimes it is informative build models which enforce ring convexity *i.e.* maintain all angles within the range $0 \leq \theta_{ijk} \leq \pi$. This can be achieved by augmenting the simplified Keating potential with a restricted bending (ReB) potential [104]:

$$\mathcal{U}(\mathbf{r}) = \frac{K_S}{2} \sum_{\substack{i,j\in \\ \text{stretches}}} \left(r_{ij} - r_0\right)^2 + \frac{K_A}{2} \sum_{\substack{i,j,k\in \\ \text{angles}}} \frac{\left(\cos\theta_{ijk} - \cos\theta_0\right)^2}{\sin^2\theta_{ijk}} . \quad (1.23)$$

The addition of the sine term in denominator causes the potential to diverge as bond angles approach linearity, preventing bonds from "inverting".

1.2.3 Geometry Optimisation

The purpose of geometry optimisation is to minimise the overall potential energy of a network, $\mathcal{U}(\mathbf{r})$, as a function of all atomic positions, $\mathbf{r}$, after they have been perturbed *e.g.* by a bond transposition. As all initial configurations are well relaxed and perturbations relatively small, this can be achieved with a local minimisation

routine. In addition as the potential models in this work are smooth and harmonic, a straightforward steepest descent algorithm is both sufficient and efficient.

The steepest descent algorithm is an iterative method which searches down the potential energy gradient until a minimum is reached [105]. It has the following scheme:

1. Calculate the potential energy of the system $\mathcal{U}_i = \mathcal{U}(\mathbf{r}_i)$
2. Determine the negative gradient of the potential *i.e.* the forces acting on the particles $\mathbf{F}_i = -\nabla\mathcal{U}_i$
3. Find the optimal distance to displace the particles along the lines of force $\mathcal{U}_{i+1} = \min\left[\mathcal{U}(\mathbf{r}_i + \lambda\mathbf{F}_i)\right]$
4. Set $\mathbf{r}_{i+1} = \mathbf{r}_i + \lambda_{\min}\mathbf{F}_i$
5. Evaluate convergence and repeat steps 1-4 if $|\mathcal{U}_{i+1} - \mathcal{U}_i| > \gamma$

The calculation of forces in stage 2 will depend on the potential model used, details of which are given in appendix **??**. Note that stage 3 also requires a minimisation routine, which may seem counter-intuitive. However, this is a one-dimensional minimisation which trivial to estimate with a line search method appendix? . The tightness of the convergence condition is set through the parameter γ.

One final performance improvement arises from the fact that the Monte Carlo are inherently local. Therefore geometry optimisation can be employed such that only the atoms in the immediate vicinity of the switching move need to be minimised to obtain an accurate structure. Typically this would extend to all atoms within five coordination shells of those directly involved in the switch move [106].

1.3 Hard Particle Monte Carlo

Hard particle Monte Carlo is one of the most well-established computational methods in statistical physics. Through its simplicity it is able to provide insight into the fundamental behaviour of particle systems and simulations of increasing size are

still performed this century [107–110]. In this thesis it will be used to generate ring systems in the form of Voronoi tessellations (see section 1.3.3), in analogy to experimental colloidal systems [50].

1.3.1 Hard Particle Model

Hard particle models are applicable over a range of dimensions. In two dimensions the system consists of an arrangement of hard disks and in three dimensions hard spheres. One can also take a quasi two-dimensional system, which comprises hard spheres confined to a plane. Regardless of the dimensionality, the central principle is that no two particles in the system can have any degree overlap. Formally, if the particle radii are denoted by R_i and the distance between any pair of particle centres by r_{ij}, the pair potential is:

$$\mathcal{U}_{ij} = \begin{cases} \infty & r_{ij} < R_i + R_j \\ 0 & \text{otherwise} \end{cases} . \tag{1.24}$$

As the total energy is simply then

$$\mathcal{U}(\mathbf{r}) = \sum_{i<j} \mathcal{U}_{ij} , \tag{1.25}$$

it follows that if any pair of particles have overlap the system energy is infinite and the Boltzmann weighting is zero. Hard particle models are typically quantified in terms of the packing fraction, ϕ, which in two dimensions has the form

$$\phi_{2D} = \rho\pi\langle R^2 \rangle , \tag{1.26}$$

where $\rho = \mathcal{N}/V$, the number density.

1.3.2 Algorithmic Details

Hard particle systems can be simulated using the Metropolis algorithm outlined in section 1.1.4. The system is initialised by selecting a random non-overlapping configuration. This can be achieved easily for low to medium densities by a greedy algorithm like random sequential addition, where particles are added successively in a manner which does not overlap with any previous particles [111]. For higher packing fractions a more sophisticated algorithm is needed Find refs .

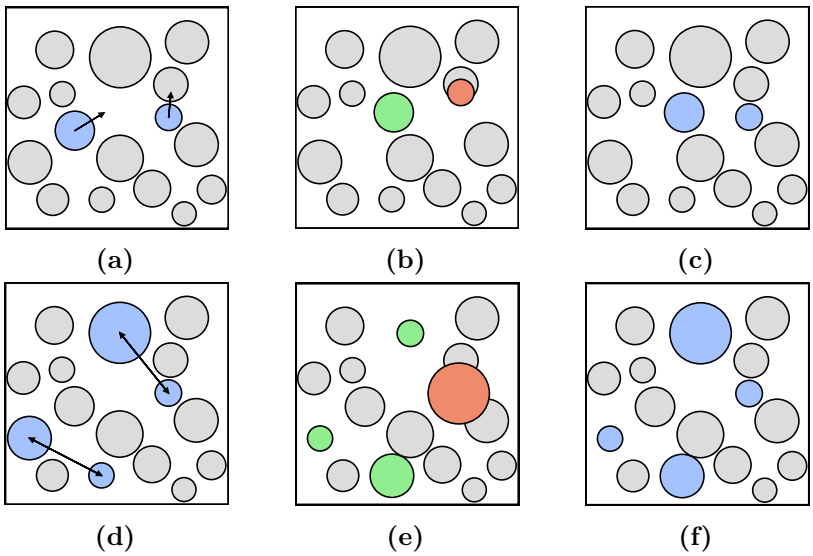

Figure 1.4: Demonstration of two displacement (a)-(c) and two swap (d)-(f) moves in hard particle Monte Carlo. In displacement moves, particles are randomly selected and assigned a trial random displacement vector (a). In swap moves, two particles are randomly selected and their radii trial swapped (b). The trial move is then examined to see if it introduces any particle overlaps (b),(e). If there are no overlaps (green), then the trial move is accepted and the system updated but otherwise (red) the move is rejected and the system returns to the previous state (c),(f).

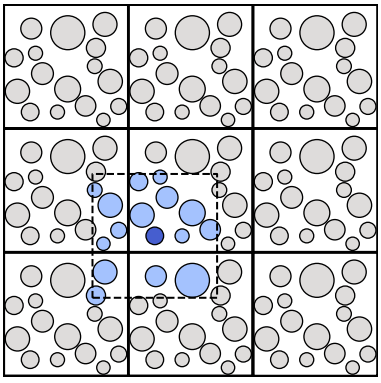

Figure 1.5: Simulation of bulk system is achieved using periodic boundary conditions, where a central cell is surrounded by repeated images of itself. A particle of interest (dark blue) then interacts with the nearest images of every other particle (light blue).

Once the initial configuration has been generated, it is evolved via two Monte Carlo moves. The first is the displacement move, whereby a random particle is selected and translated according to a random vector with elements generated uniformly in the range $[-\delta, \delta]$. If the displacement introduces any particle overlaps it is rejected, otherwise the system is updated to the new configuration, as illustrated in

figure 1.4a-1.4c. The value of δ is chosen for each simulation such that the proportion of accepted moves is $\sim 50\%$, allowing for efficient searching of configurational space. The optimal value can be determined by continuous adjustment during equilibration.

The second is the swap move, where two random particles are selected their radii exchanged [112, 113]. Once again a swap move is only accepted if it does not lead to any overlapping particles and is demonstrated in figure 1.4d-1.4f. The swap move is used to increase the efficiency in simulations of polydisperse particles and is an example of how the design of Monte Carlo moves can be flexible and they do not have to have a direct physical basis. The swap move is attempted for every ten displacement moves.

Finally, to remove the presence of an interface in the system, simulation is performed with periodic boundary conditions. In this scheme the central simulation cell is repeated to form an infinite lattice, so that every particle experiences a bulk environment. Coupled with this is the use of the minimum image convention, where each particle then only interacts with the nearest repeated image of all the remaining particles. This is illustrated in figure 1.5.

1.3.3 Voronoi Construction

The hard particle configurations produced by Monte Carlo simulations are not in themselves network structures, rather simply a collection of correlated points. The network structure is revealed by construction of a Voronoi diagram, which partitions the sample into a system of tessellating cells, where each cell encapsulates all the space closest to the associated particle [114]. A two-dimensional Voronoi diagram is formed through the placement of dividing lines between the centres of neighbouring particles. The intersection of these lines forms the characteristic tessellating polygons.

In the simplest unweighted approach, the dividing line between two neighbouring particles separated by the Euclidean distance r_{ij}, is simply located midway between the particles at a distance $r_{ij}/2$. The elegance of the unweighted Voronoi diagram is that only the particle centres are required for its construction, with no requirement

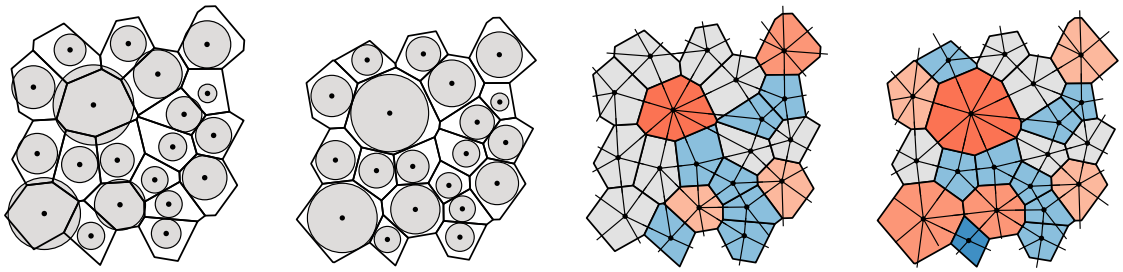

Figure 1.6: Voronoi construction of a polydisperse hard disk system. Panels (a) and (b) compare the unweighted and weighted (radical) Voronoi tessellations respectively. The radical Voronoi assigns more volume to the larger particles to ensure a more equitable distribution of space, which can affect the underlying ring structure, shown in panels (c) and (d). The dual network, known as the Delaunay triangulation, is also overlaid.

for a cut-off parameter. Whilst the unweighted Voronoi tessellation is very effective for studying monodisperse particles, there are some limitations for polydisperse species. Specifically, the Voronoi partition underestimates the space assigned to large particles and overestimates that for small particles - a simple reflection of the lack of information on particle radii (see figure 1.6a). To rectify this, weighted modifications have been suggested which take account of the differences in radii [115].

To construct a weighted Voronoi diagram, one simply adjusts the position of the dividing line, such that it is further from the particle with the greater weight. The weighting method used in this work is the so called radical tessellation introduced by Finney [116]. In this modification, the dividing line is placed a distance d_i from particle i, given by:

$$d_i = \frac{w_i^2 - w_j^2 + r_{ij}^2}{2r_{ij}}\,, \tag{1.27}$$

where w_i and w_j are the weights for each particle. The benefit of this method is that is adjusts the partitioning of space so that greater volume is assigned to the particles with larger weight, and is well designed so that all of the sample space remains accounted for - unlike some alternative constructions [117]. In terms of the particle weights, the logical choice is simply the disk radii. This is because at the contact distance, $r_{ij} = R_i + R_j$, equation (1.27) shows that $d_i = R_i$ *i.e.* the radical dividing line sits exactly between the two disks, producing the most equitable distribution

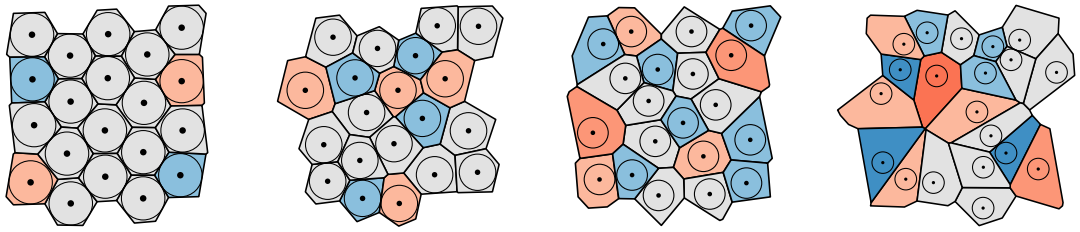

(a) $\phi = 0.8$ **(b)** $\phi = 0.6$ **(c)** $\phi = 0.4$ **(d)** $\phi = 0.2$

Figure 1.7: The ring structure in Voronoi diagrams is controlled through the packing fraction, ϕ, of the underlying hard particle system. Ring diversity increases as packing fraction is lowered from $0.8 \rightarrow 0.2$ in (a)-(d).

of volume (see figure 1.6b). Furthermore, when the radii are equal, $d_i = r_{ij}/2$ and the result from the standard unweighted Voronoi is regenerated as expected. It is worth noting here that the weighting method can affect the ring sizes (*i.e.* number of vertices) as well as the ring areas, as demonstrated in figures 1.6c,1.6d.

The outcome of the Voronoi construction is a system of percolating rings not dissimilar to those seen in materials. The dual network, known as the Delaunay triangulation, is also obtained, which defines the nearest neighbours for each particle. The main difference with atomic materials is that the polygon edge lengths and angles are not constrained by a potential model the ring structure is therefore completely entropically controlled. The degree of disorder is then determined by the packing fraction, ϕ, where decreasing the packing fraction leads to increased diversity in the ring statistics, as illustrated in figure 1.7. As can be seen there are some defects which are analogous to those seen in materials, such as the Stone-Wales defect in figure 1.7b, but others are not, as in figure 1.7a which arise from very small perturbations in the crystalline lattice. The limiting value as $\phi \rightarrow 0$ is well studied as the Poisson Voronoi diagram [118, 119]. This corresponds to the Voronoi diagram formed from a random uniform array of points. In this way Voronoi systems provide a good complement to compare and contrast with materials.

1.4 Analysis Methods

1.4.1 Bond Length and Angle Distributions

1.4.2 Radial Distribution Functions

2 | Voronoi Analysis of Quasi-Two-Dimensional Hard Spheres

Experimental investigations have led to the synthesis of colloidal monolayers, where particles are sedimented on a surface, creating effective quasi-two-dimensional hard sphere systems. Voronoi diagrams are constructed for a range of configurations of such systems, generated from both experiment and computation. The evolution in the network properties with packing fraction is explored with packing fraction for mono-, bi- and polydisperse particle systems. A detailed comparison is presented of unweighted and weighted variants of the Voronoi construction in the context of quasi-two-dimensional systems. It is shown that the two-dimensional unweighted Voronoi, favoured in experimental analyses, has a well-defined physical interpretation, corresponding to the basal section of a three-dimensional weighted Voronoi. In addition the stereology of the three-dimensional Voronoi is examined and constrasted with equivalent systems of hard disks.

2.1 Quasi-2D Hard Sphere Systems

Hard particle models are a central tenet of statistical physics, forming the basis of fundamental research dating from the earliest computations to current research [107]. This is because, despite their simplicity, the hard disk and hard sphere models are able to explain many of the behaviours of classical particles in two and three dimensions. In particular, these models effectively complement the study of colloids [174]. The interest in colloids themselves stems from the fact that they occupy a "sweet-spot", in that the particles are large enough to observe

with confocal microscopy, whilst being small enough that their motion is governed by simple fundamental forces on a reasonable time scale. It is therefore possible to track and visualise particle positions in real-time, also making them an good proxy for classical atomic systems.

The hard particle model was introduced in section 1.3.1, in the context of hard disks and hard spheres, which, as mentioned, have been extensively studied in the literature. However, section **??** introduced a new system of recent experimental interest, that of a monolayer of hard spheres. These systems, where colloidal particles are sedimented on a plane in a single layer, are three-dimensional (3D) systems with effectively two-dimensional (2D) interactions. As such, they are termed quasi-two-dimensional (quasi-2D). In section1.3.1, all monolayers comprised spheres of the same size, but one can equally engineer systems where the sphere radii have a distribution of sizes *i.e.* different size dispersity [175, 176]. In the polydisperse case, the centres of the spheres no longer lie in the same plane, but rather at a height equal to their radius. The result of this dispersity is that the interaction distances between particles of different sizes cannot be trivially projected into 2D. Nevertheless, it is still possible to model monolayers of spheres in 2D by using non-additive distances. For two particles in a quasi-2D arrangement with radii, R_i, the contact distance in 2D, R_{ij}, is related to the geometric mean of the radii:

$$R_{ij} = 2\left(R_i R_j\right)^{1/2} , \tag{2.1}$$

as illustrated for two spheres, A, B, in figure 2.1. Alternatively, this can be expressed in terms the arithmetic mean and a non-additivity parameter, Δ, as is common for asymmetric systems [177]:

$$R_{ij} = \left(R_i + R_j\right)\left(1 + \Delta\right) , \tag{2.2}$$

where

$$\Delta = \frac{2\left(R_i R_j\right)^{1/2}}{R_i + R_j} - 1 . \tag{2.3}$$

This allows quasi-2D systems to be modelled purely in 2D.

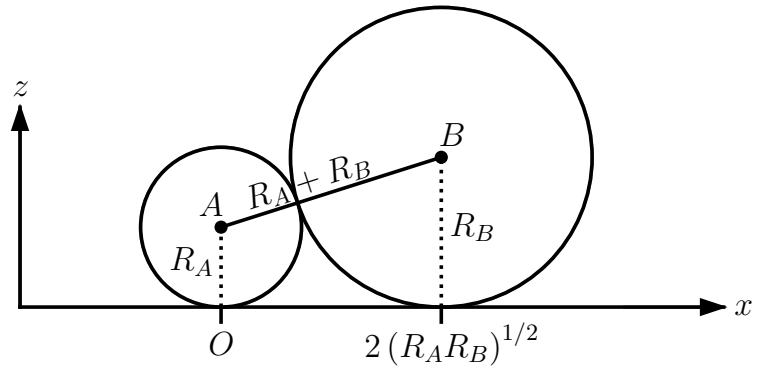

Figure 2.1: Quasi-2D hard spheres can be modelled in 2D by using non-additive interaction distances. Here two spheres sedimented on a plane have a contact distance given by twice the geometric mean of the radii.

Since systems of colloidal monolayers can be treated as a 2D problem, this should enable them to be analysed with a 2D Voronoi diagram. Voronoi analysis allows determination of the coordination environments around each particle, so that network properties such as the neighbour degree distribution and correlations can be calculated [32, 158, 178, 179]. This information can be used, for example, to give insights as to the phase behaviour in these systems [50, 180–182]. However, it is not initially clear how the non-additivity will affect the calculation of the Voronoi diagram. For instance, unlike a system of additive hard disks, it is not obvious if a unweighted or weighted variant of the Voronoi construction is most appropriate, and in the latter case what the weightings should be. It will be demonstrated in the second half of this chapter that in fact the unweighted construction retains a precise physical meaning for quasi-2D systems, and is the natural choice for partitioning space in these monolayers.

2.1.1 Experimental Analysis

Raw experimental coordinates were kindly provided for a range of mono- and bidisperse colloidal systems by Thorneywork and Dullens [50, 175, 183]. The colloidal monolayers were prepared by dispersing particles of specific radii in a water-ethanol mixture and sedimenting them on the base of a glass sample cell. The samples were then imaged using an inverted bright-field microscope and particle coordinates obtained using standard particle tracking routines. Allowing a time

Table 2.1: Summary of the experimental parameters which can be controlled in colloidal monolayers.

	Mono	Binary		
		Large	Small	Total
Radius	R	R_l	R_s	-
Radius ratio	1	-	-	$\gamma = R_l/R_s$
Composition	1	c_l	c_s	1
Number density	ρ	$\rho_l = c_l\rho$	$\rho_s = c_s\rho$	$\rho = \rho_l + \rho_s$
Packing fraction	$\phi = \rho\pi R^2$	$\phi_l = \rho_l\pi R_l^2$	$\phi_s = \rho_s\pi R_s^2$	$\phi = \phi_l + \phi_s$

of around $10s$ between frames ensured that the particle positions are sufficiently decorrelated to be statistically independent.

Data was made available across a range of experimental conditions. For the monodisperse systems, samples contained particles with radii of $R = 1.395\mu$m, across a range of 2D packing fractions, ϕ, as defined in equation ref . For bidisperse systems, which consist of two particle sizes, one "large" and the other "small", there are more free parameters to control, which are summarised in table 2.1. Firstly there is the radius ratio of the particles, $\gamma = R_l/R_s$ (the subscripts "l" and "s" will be used to denote variables corresponding to large and small particles respectively), which relates the relative particle sizes. Secondly, the composition, c_l, c_s, determines the proportion of each particle type, where $c_l + c_s = 1$. Finally there is also the packing fraction, calculated with reference to one of the components ϕ_l, ϕ_s, or using all particles to give a total packing fraction $\phi = \phi_l + \phi_s$. For completeness, it is noted that the composition can also be represented by ϕ_l/ϕ, but for the purposes of this work the definition above was found to be more intuitive. The available experimental data contained systems at two radius ratios and a variety of compositions and packing fractions. More specifically, these had either $R_s = 1.395\mu$m and $R_l = 3.05, 2.02\mu$m, corresponding to size ratios of $\gamma = 2.19, 1.45$ respectively. In addition for each set of experimental conditions there were 100 configurations, which the exact compositions and packing fractions for each were determined and presented in table 2.2

Table 2.2: Details of experimental colloidal samples. Samples are defined in terms of particle size dispersity, particle radius ratio, composition and total packing fraction. The mean value is supplied for each, with the standard deviation given in brackets.

Mono	Binary, $\gamma = 2.19$		Binary, $\gamma = 1.45$		Binary, $\gamma = 1.45$	
ϕ	c_l	ϕ	c_l	ϕ	c_l	ϕ
0.655(1)	0.201(1)	0.764(2)	0.532(4)	0.571(1)	0.233(1)	0.607(2)
0.616(1)	0.182(1)	0.639(2)	0.522(4)	0.477(4)	0.208(1)	0.406(1)
0.509(1)	0.192(2)	0.507(3)	0.543(5)	0.267(1)	0.226(3)	0.309(2)
0.427(1)	0.189(2)	0.339(3)	0.332(1)	0.629(1)	0.091(1)	0.663(1)
0.341(1)	0.187(7)	0.150(2)	0.314(3)	0.499(3)	0.107(1)	0.500(2)
0.289(0)			0.345(2)	0.337(2)	0.087(1)	0.257(1)

The 2D experimental coordinates can be analysed using a Voronoi construction. An example for both a mono- and bidisperse configurations can be found in figure 2.2. With the raw coordinates, the experimental samples can be treated analogously to configurations generated from computation. The only difference is that the experimental images are by nature aperiodic, and so when analysing the network properties of the Voronoi diagram, the cells close to the boundary must be neglected, to remove any edge effects. However, careful examination of figure 2.2a reveals some small imperfections in the data, as there are instances where the monodisperse particles appear to overlap. This is not a result of differences in particle size, but rather the presence of "phantom" particles deriving from the imaging process. Extracting particle positions from the experimental data is highly non-trivial, in particular removing points arising from interstitial sites between densely packed particles [183]. Whilst this becomes more problematic at higher packing fractions, they are however still few and far between. It should also be point out here that the tracking routines are able to detect the difference between large and small particles in bidisperse systems, allowing Voronoi cells to be associated to particles of a specific size. The actual results of the analysis of these experimental systems will be discussed alongside the results from computation in section ref .

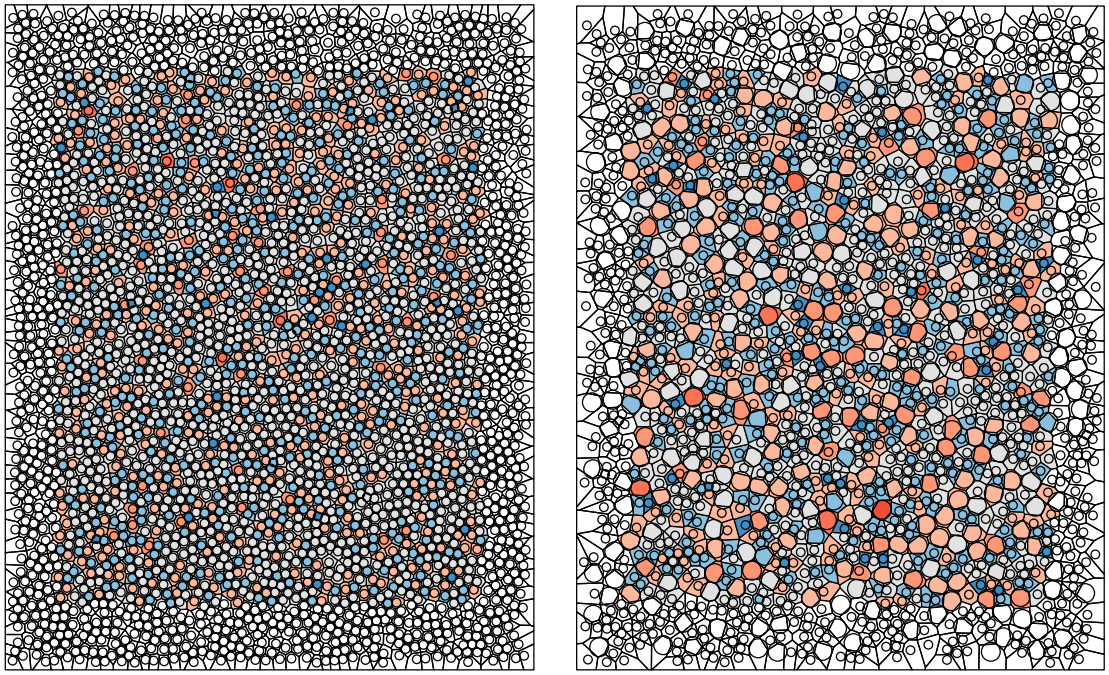

(a) Mono, $\phi = 0.509$ **(b)** Binary, $\gamma = 2.19$, $c_l = 0.192$, $\phi = 0.507$

Figure 2.2: Voronoi analysis of two example experimental snapshots, of a monodisperse and bidisperse quasi-2D colloidal monolayer (system parameters in captions). Circles indicate particles of a given radius whilst Voronoi cells are coloured according to size. Voronoi cells without shading indicates those that were neglected from network analysis due to proximity to the image boundary.

2.1.2 Non-Additive Hard Disk Monte Carlo

Experimental data can be compared and contrasted with configurations generated from simulation. Hard particle Monte Carlo was introduced in section 1.3 as a method to generate such configurations computationally. One could set up a 3D system of hard spheres constrained to a plane, but as discussed above it is preferable to employ a non-additive hard disk model. In this modification, if two particles are separated by a distance, $r_i j$, the pair potential is:

$$\mathcal{U}_{ij} = \begin{cases} \infty & r_{ij} < 2\left(R_i R_j\right)^{1/2} \\ 0 & \text{otherwise} \end{cases} . \tag{2.4}$$

The remainder of the algorithm proceeds the same as in the standard methods, as outlined in section 1.3.

For all simulations in this chapter, unless otherwise stated, $\mathcal{N} = 1000$ particles were placed in a 2D periodic box, then equilibrated with 10^5 Monte Carlo cycles

with each cycle consisting of $\mathcal{N}$ random moves. After equilibration, 10^5 Monte Carlo cycles are performed with sampling every 100 cycles. For each set of simulation parameters, averaging was carried out over 10 different random seeds.

2.2 Monodisperse Spheres

The simplest quasi-2D system to study is that of a monolayer of monodisperse spheres. This is because as all sphere radii are the same, the non-additive model reduces here to a simple additive model of hard disks. The case of monodisperse spheres has therefore already been partially explored the previous chapter. For example, sections **??** and **??** discussed the degree-distributions and assortativity in contrast with a range of other physical networks. To avoid repetition, this section will therefore focus on the network properties in terms of a measure specific to colloids, the packing fraction.

2.2.1 Network Properties with Packing Fraction

The network properties of the Voronoi diagrams in this section are again summarised by the proportion of hexagons, p_6, and the assortativity, r. As was shown in section **??**, as the ring statistics in the Voronoi diagrams of monodisperse quasi-2D colloids follow Lemaître's maximum entropy law, p_6 can also be considered a descriptor for the width of the ring distribution. The assortativity once again measures the local ring correlations. Figure 2.3a shows the results of the evolution of p_6 with ϕ, for both experiment and simulation. The first thing to note is that there is excellent agreement between the experimental system and the hard particle model, indicating that this model is indeed suitable for exploring the behaviour of colloidal monolayers. In addition, comparison is also provided to a previous computational study [179], to which again there is perfect agreement. More generally, the value of p_6 decreases with packing fraction. The hexatic phase, which exists at high packing fraction is characterised by having particles in 6-coordinate environments. Under melting, as the available volume increases, 5- and 7-ring defects are initially

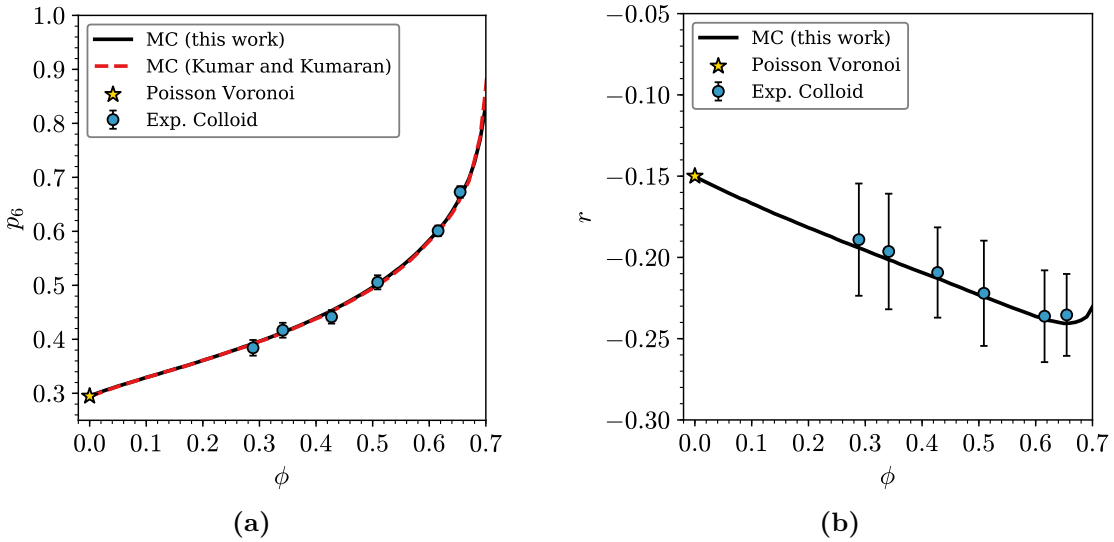

Figure 2.3: Network properties of monodisperse systems of quasi-2D hard spheres, in terms of the proportion of hexagons, panel (a), and the assortativity, panel (b). Data is presented both from simulation and experiment, with the experimental points indicating the mean value and one standard deviation. A comparison is also made in panel (a) to a previous study [179], to which there is excellent agreement.

introduced, depreciating p_6, before more extreme ring sizes manifest. Finally, in the limit of the ideal gas (as $\phi \to 0$), the Poisson Voronoi tessellation is obtained.

The behaviour of the assortativity with packing fraction is given in figure 2.3b. Once again, there is very good agreement between configurations from experiment and computation. The fluctuations in the values of r are larger than p_6, for the experimental systems. This is because.....Local measure? Mark? Strikingly, the assortativity seems to display behaviour that is linear in packing fraction, at least for intermediate values. It is not immediately clear why this should be the case, and is an interesting result that warrants more research. In addition, it can be seen that this linearity comes to an end around $\phi \approx 0.66$, with r displaying a sudden upturn. This point is close to the limit of the liquid phase for hard disks, before it undergoes transition to a hexatic phase [50]. This phase transition seems to be captured clearly through the assortativity.

Check all this with Mark

2.3 Bidisperse Spheres

Monolayers of bidisperse spheres present a natural extension to the monodisperse case, and come with the advantage of having available experiment information for comparison. In this section the ring statistics of bidisperse systems will be explored, with a focus on systems matching the experimental parameters, as outlined in table 2.2. Owing to the fact that there are two types of particle present (which experimental imaging is able to differentiate), metrics in this section will be considered in reference to both large and small particles. To this point, the ring statistics can then be divided into partial ring distributions for each particle type, denoted p_k^l and p_k^s. A subtle but important point is that the mean ring sizes for these partial distributions ($\langle k \rangle_l$ and $\langle k \rangle_s$) are no longer constrained to be six. Instead it is their weighted sum which is constrained by Euler's formula such that:

$$c_l \langle k \rangle_l + c_s \langle k \rangle_s = \langle k \rangle = 6\,. \tag{2.5}$$

The mean ring sizes can then take values either side of six, quantifying the relative coordination numbers of the particles of different sizes.

In this section systems of two radius ratios will be discussed: the first with $\gamma = 1.45$, termed the small size ratio; the second with $\gamma = 2.09$, termed the large size ratio. The primary focus will however be on the small size ratio, as this is complemented by the most experimental data. The overarching properties of the ring structure will first be explored, before the explicit ring statistics are again examined in relation to a maximum entropy solution.

2.3.1 Ring Statistics with Packing Fraction

The mean values of the partial ring distributions for large and small spheres are given for the bidisperse systems of both radius ratios in figures 2.4a, 2.4b. Beginning with the small size ratio ($\gamma = 1.45$, figure 2.4a), it can be seen that there is once again good agreement with the experimental data. With the aid of the Monte Carlo simulations, it is clear that these experimental points actually lie on a series of curves. To rationalise the broad behaviour of these curves, one can begin by noting

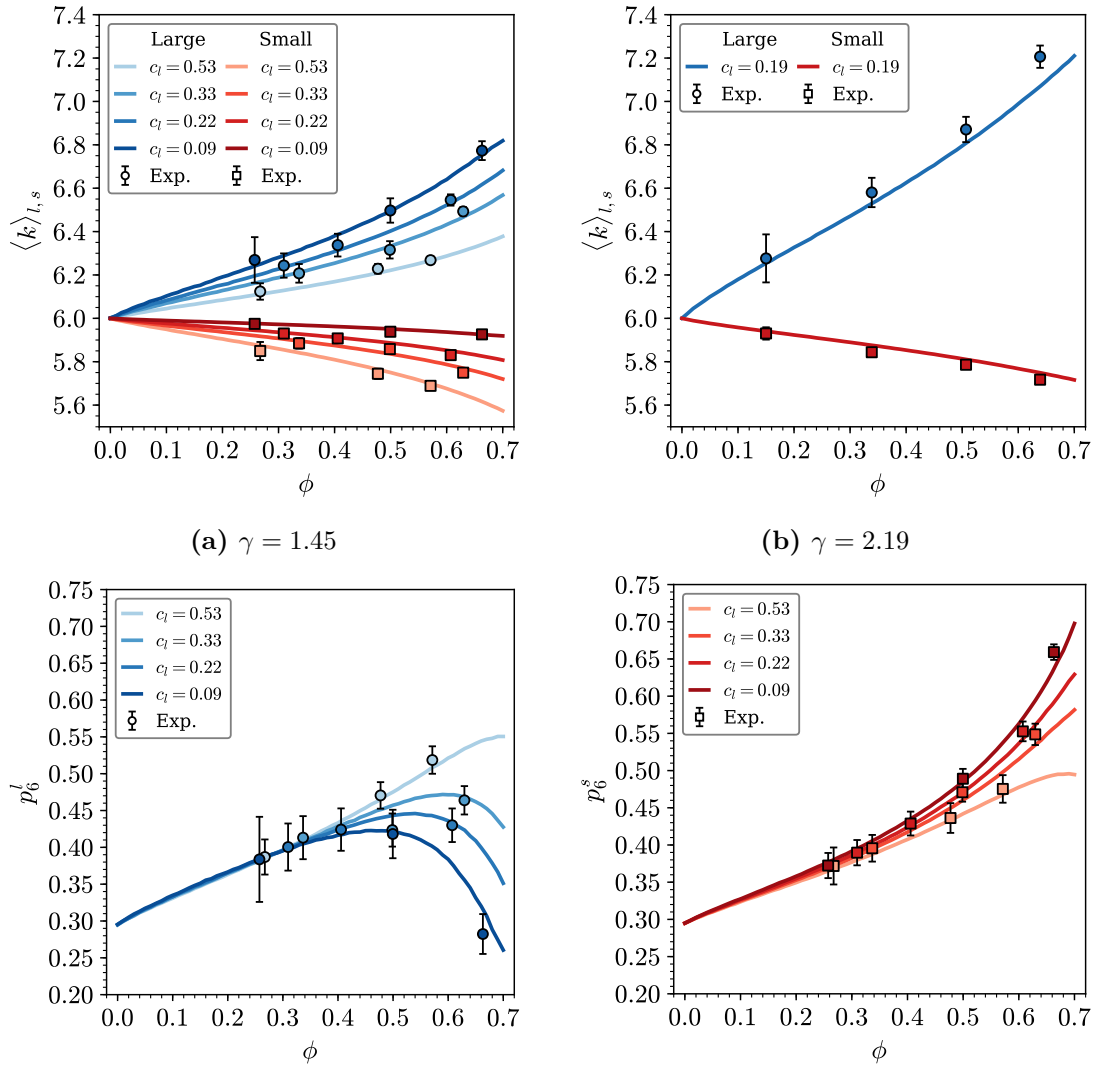

(a) $\gamma = 1.45$

(b) $\gamma = 2.19$

(c) $\gamma = 1.45$, Large Spheres

(d) $\gamma = 1.45$, Small Spheres

Figure 2.4: Overview of the evolution in the partial ring statistics in bidisperse colloidal monolayers. Panels (a),(b) show the partial mean sizes for the two radius ratios (as indicated in captions). Panels (c),(d) show the proportion of hexagons in the partial distributions for the $\gamma = 1.45$ systems. The blue curves correspond to quantities pertaining to large particles, red curves to small particles. The system composition is indicated by the depth of shading, as in the legends. Experimental points are coloured using the same scale as for simulation curves, and error bars indicate one standard deviation of the mean.

that $\langle k \rangle_l > 6$ and $\langle k \rangle_s < 6$ for all values of $\phi > 0$. This is simply an expression of the fact that larger spheres will always have on average more nearest neighbours than smaller spheres. Following this observation, it can be seen that $\langle k \rangle_l$ increases as the fraction of large particles decreases, for a fixed packing fraction. This is a due to large spheres having statistically fewer large sphere neighbours the lower

the concentration c_l. Each large particle can accommodate more particles around it, the greater the dilution of small particles. As a further illustration, one can consider a large sphere in a "sea" of small spheres ($c_l \to 0$). Here the large particle nearest neighbours must be maximised and equally the small particles only interact with other small particles. As such the mean coordination for the small particles must approach the average of six. This reciprocal behaviour of small spheres also explains the trend in $\langle k \rangle_s$, which approaches the horizontal limit of $\langle k \rangle_s = 6$ as $c_l \to 0$. Once again the effect of decreasing packing fraction is to diminish the effects of relative sphere size, as the excluded volume is lower, until eventually the random limit is reached. Come up with a satisfactory relative model for this? Perhaps I have a semi-decent one somewhere...

The analogous data is also presented for the large size ratio system in figure 2.4b. Here it can be seen that similar trends hold for $\langle k \rangle_l$ and $\langle k \rangle_s$ as discussed for the small size ratio above. However, the increased size differential leads to even more extreme differences in the partial mean ring sizes. For example, for the large size ratio with $c_l = 0.19$, $\langle k \rangle_l \approx 7.21$ but for the small size ratio with $c_l = 0.22$, $\langle k \rangle_l \approx 6.68$. It should be noted that the fit with experiment is less accurate for the large size ratio spheres, a problem that is particularly pronounced at higher packign fractions. This suggests two possible inadequacies. Either the hard particle model is insufficient, and there are some additional short range interactions which become non-negligible at higher packing fractions, or the difficulties in directly imaging the particles become more significant.

The proportion of hexagons for each subsystem is also plotted in terms of the packing fraction in figures 2.4d, **??**, for the spheres with small size ratio. Again, even at this more fine-grained level, the correlation with experimental data remains strong. The results for the small spheres in figure **??** reflect a general trend regularly seen in this thesis, where the number of hexagons is maximised as ordering increases with higher packing fraction, and again the p_6 increases as the number of disrupting large spheres decreases. The results for the large spheres in figure 2.4d are somewhat more dramatic, with p_6 displaying a maximum with changing packing. This will be

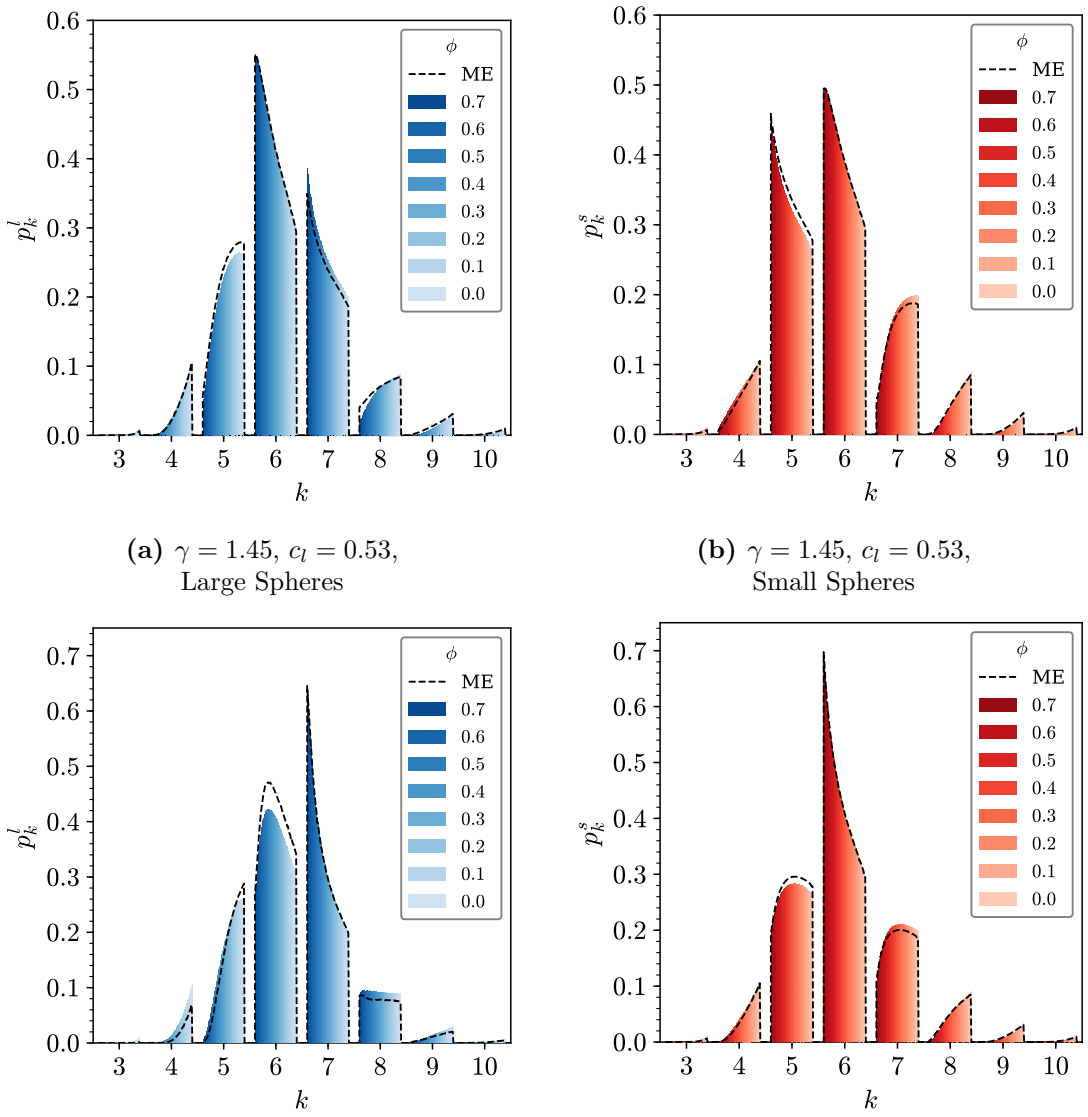

(a) $\gamma = 1.45$, $c_l = 0.53$, Large Spheres

(b) $\gamma = 1.45$, $c_l = 0.53$, Small Spheres

(c) $\gamma = 1.45$, $c_l = 0.09$, Large Spheres

(d) $\gamma = 1.45$, $c_l = 0.09$, Small Spheres

Figure 2.5: Variation of partial ring distributions with packing fraction for two different compositions of a $\gamma = 1.45$ bidisperse monolayer, contrasted with maximum entropy solutions. Left panels show the statistics for rings associated with larger particles, and right panels with smaller particles. The maximum entropy solutions are overlaid as dashed lines for comparison.

discussed to greater extent in the following section, but essentially results from the hexagon no longer being the dominant ring size, begin replaced by the heptagon. Similar trends were in fact seen for x-rings in triangle rafts in section ref .

2.3.2 Maximum Entropy Solutions

Is this figure clear or confusing?

2.3.3 Network Properties

2.4 Polydisperse Spheres

2.4.1 Network Properties

2.5 Chapter Summary

Appendices

References

[1] W H Zachariasen. “The Atomic Arrangement in Glass”. In: *J. Am. Chem. Soc.* 54.10 (1932), pp. 3841–3851.

[2] J. Kotakoski et al. “From point defects in graphene to two-dimensional amorphous carbon”. In: *Phys. Rev. Lett.* 106 (2011), p. 105505.

[3] Alex W. Robertson et al. “Spatial control of defect creation in graphene at the nanoscale”. In: *Nat. Commun.* 3 (2012), p. 1144.

[4] Pinshane Y Huang et al. “Direct Imaging of the a Two-Dimensional Silica Glass on Graphene”. In: *Nano Lett.* 12 (2012), pp. 1081–1086.

[5] Leonid Lichtenstein, Markus Heyde, and Hans Joachim Freund. “Atomic arrangement in two-dimensional silica: From crystalline to vitreous structures”. In: *J. Phys. Chem. C* 116 (2012), pp. 20426–20432.

[6] Shamil Shaikhutdinov and Hans-joachim Freund. “Metal-Supported Aluminosilicate Ultrathin Films as a Versatile Tool for Studying the Surface Chemistry of Zeolites”. In: *ChemPhysChem* 14 (2013), pp. 71–77.

[7] Adrián Leandro Lewandowski et al. “Atomic structure of a metal-supported two-dimensional germania film”. In: *Phys. Rev. B* 97 (2018), p. 115406.

[8] L Lewandowski et al. “From Crystalline to Amorphous Germania Bilayer Films at the Atomic Scale: Preparation and Characterization”. In: *Angew. Chem. Int. Ed.* 58 (2019), pp. 10903–10908.

[9] Panagiotis Trogadas, Thomas F Fuller, and Peter Strasser. “Carbon as catalyst and support for electrochemical energy conversion”. In: *Carbon N. Y.* 75 (2014), pp. 5–42.

[10] Yongfu Sun et al. “Ultrathin Two-Dimensional Inorganic Materials : New Opportunities for Solid State Nanochemistry”. In: *Acc. Chem. Res.* 48 (2015), pp. 3–12.

[11] Christin Büchner and Markus Heyde. “Two-dimensional silica opens new perspectives”. In: *Prog. Surf. Sci.* 92 (2017), pp. 341–374.

[12] Paul A Beck. “Annealing of cold worked metals”. In: *Adv. Phys.* 3.11 (1954), pp. 245–324.

[13] C G Dunn and E F Koch. “Comparison of Dislocation Densities of Primary and Secondary Recrystallization Grains of Si-Fe”. In: *Acta Metall.* 5 (1957), p. 548.

[14] A J Stone and D J Wales. “Theoretical Studies of Icosahedra C60 and Some Related Species”. In: *Chem. Phys. Lett.* 128.5,6 (1986), pp. 501–503.

[15] J. Shackelford and B. D. Brown. “The Lognormal Distribution in the Random Network Structure”. In: *J. Non. Cryst. Solids* 44 (1981), pp. 379–382.

[16] J Lemaitre et al. “Arrangement of cells in Voronoi tesselations of monosize packing of discs”. In: *Philos. Mag. B* 67.3 (1993), pp. 347–362.

[17] Leonid Lichtenstein et al. “The atomic structure of a metal-supported vitreous thin silica film”. In: *Angew. Chemie - Int. Ed.* 51 (2012), pp. 404–407.

[18] D A Aboav. “Arrangement of grains in a polycrystal”. In: *Metallography* 3 (1970), pp. 383–390.

[19] D. Weaire. “Some remarks on the arrangement of grains in a polycrystal”. In: *Metallography* 7 (1974), pp. 157–160.

[20] Torbjörn Björkman et al. “Defects in bilayer silica and graphene: Common trends in diverse hexagonal two-dimensional systems”. In: *Sci. Rep.* 3 (2013), p. 3482.

[21] Andrei Malashevich, Sohrab Ismail-Beigi, and Eric I. Altman. “Directing the structure of two-dimensional silica and silicates”. In: *J. Phys. Chem. C* 120 (2016), pp. 26770–26781.

[22] Mark Wilson et al. “Modeling vitreous silica bilayers”. In: *Phys. Rev. B* 87 (2013), p. 214108.

[23] Mark Wilson and Harry Jenkins. “Crystalline thin films of silica : modelling , structure and energetics”. In: *J. Phys. Condens. Matter* 30 (2018), p. 475401.

[24] Jin Zhang. “Phase-dependent mechanical properties of two-dimensional silica films: A molecular dynamics study”. In: *Comput. Mater. Sci.* 142 (2018), pp. 7–13.

[25] Franz Bamer, Firaz Ebrahem, and Bernd Markert. “Athermal mechanical analysis of Stone-Wales defects in two-dimensional silica”. In: *Comput. Mater. Sci.* 163 (2019), pp. 301–307.

[26] Projesh Kumar Roy and Andreas Heuer. “Ring Statistics in 2D Silica: Effective Temperatures in Equilibrium”. In: *Phys. Rev. Lett.* 122 (2019), p. 016104.

[27] Nina F. Richter et al. “Characterization of Phonon Vibrations of Silica Bilayer Films”. In: *J. Phys. Chem. C* 123 (2019), pp. 7110–7117.

[28] Projesh Kumar Roy, Markus Heyde, and Andreas Heuer. “Modelling the atomic arrangement of amorphous 2D silica: a network analysis”. In: *Phys. Chem. Chem. Phys.* 20 (2018), pp. 14725–14739.

[29] Avishek Kumar et al. “Ring statistics of silica bilayers”. In: *J. Phys. Condens. Matter* 26 (2014), p. 395401.

[30] D. A. Aboav. “The arrangement of cells in a net. I”. In: *Metallography* 13 (1980), pp. 43–58.

[31] B. N. Boots. “Comments on "Aboav’s Rule" for the Arrangement of Cells in a Network”. In: *Metallography* 17 (1984), pp. 411–418.

[32] J. C. Earnshaw and D. J. Robinson. “Topological correlations in colloidal aggregation”. In: *Phys. Rev. Lett.* 72.23 (1994), p. 3682.

[33] C Allain and L Limat. “Regular Patterns of Cracks Formed by Directional Drying of a Collodial Suspension”. In: *Phys. Rev. Lett.* 74.15 (1995), p. 2981.

[34] A Moncho-Jorda, F Martinez-Lopez, and R Hidalgo-Alvarez. "Simulations of aggregation in 2D . A study of kinetics , structure and topological properties". In: *Physica A* 282 (2000), pp. 50–64.

[35] Marc Durand et al. "Statistical mechanics of two-dimensional shuffled foams: Prediction of the correlation between geometry and topology". In: *Phys. Rev. Lett.* 107 (2011), p. 168304.

[36] Mingming Tong et al. "Geometry and Topology of Two-Dimensional Dry Foams : Computer Simulation and Experimental Characterization". In: *Langmuir* 33 (2017), pp. 3839–3846.

[37] Lucas Goehring and Stephen W Morris. "Cracking mud, freezing dirt, and breaking rocks". In: *Phys. Today* 67.11 (2014), p. 39.

[38] D Brutin et al. "Pattern formation in drying drops of blood". In: *J. Fluid Mech.* 667 (2011), pp. 85–95.

[39] Franziska Glassmeier and Graham Feingold. "Network approach to patterns in stratocumulus clouds". In: *PNAS* 114.40 (2017), pp. 10578–10583.

[40] Michel C Milinkovitch et al. "Crocodile Head Scales Are Not Developmental Units But Emerge From Physical Cracking". In: *Science (80-.).* 339 (2019), pp. 78–81.

[41] G. Le Caër and R. Delannay. "The administrative divisions of mainland France as 2D random cellular structures". In: *J. Phys. Fr.* 3 (1993), p. 1777.

[42] G Schliecker and S Klapp. "Why are the equilibrium properties of two-dimensional random cellular structures so similar?" In: *Europhys. Lett.* 48.2 (1999), pp. 122–128.

[43] William T. Gibson et al. "Control of the mitotic cleavage plane by local epithelial topology". In: *Cell* 144 (2011), pp. 427–438.

[44] M Kokalj Ladan, P Ziherl, and A Šiber. "Topology of dividing planar tilings : Mitosis and order in epithelial tissues". In: *Phys. Rev. E* 100 (2019), p. 012410.

[45] D. Weaire and N. Rivier. "Soap, cells and statistics-random patterns in two dimensions". In: *Contemp. Phys.* 50.1 (2009), pp. 199–239.

[46] J C Flores. "Mean-field crack networks on desiccated films and their applications : Girl with a Pearl Earring". In: *Soft Matter* 13 (2017), pp. 1352–1356.

[47] Steven H Strogatz. "Exploring complex networks". In: *Nature* 410 (2001), p. 268.

[48] S Boccaletti et al. "Complex networks : Structure and dynamics". In: *Phys. Rep.* 424 (2006), pp. 175–308.

[49] Albert-László Barabási. "The network takeover". In: *Nat. Phys.* 8 (2012), pp. 14–16.

[50] Alice L. Thorneywork et al. "Two-Dimensional Melting of Colloidal Hard Spheres". In: *Phys. Rev. Lett.* 118 (2017), p. 158001.

[51] Andrew B Cairns et al. "Design of crystal-like aperiodic solids with selective disorder–phonon coupling". In: *Nat. Commun.* 7 (2016), p. 10445.

[52] Albert-László Barabási and Márton Pósfai. *Network science*. Cambridge: Cambridge University Press, 2016.

[53] Xianglong Yuan and A N Cormack. “Efficient algorithm for primitive ring statistics in topological networks”. In: *Comput. Mater. Sci.* 24 (2002), pp. 343–360.

[54] D. A. Aboav. “The Arrangement of Cells in a Net. III”. In: *Metallography* 17 (1984), pp. 383–396.

[55] E Ressouche et al. “Magnetic Frustration in an Iron-Based Cairo Pentagonal Lattice”. In: *Phys. Rev. Lett.* 103 (2009), p. 267204.

[56] P W Fowler et al. “Energetics of Fullerenes with Four-Membered Rings”. In: *J Phys Chem* 100 (1996), pp. 6984–6991.

[57] A. Gervois, J. P. Troadec, and J. Lemaitre. “Universal properties of Voronoi tessellations of hard discs”. In: *J. Phys. A* 25 (1992), pp. 6169–6177.

[58] G. Le Caër and R. Delannay. “Correlations in Topological Models of 2d Random Cellular Structures”. In: *J. Phys. A* 26 (1993), pp. 3931–3954.

[59] P Cerisier, S Rahal, and N Rivier. “Topological correlations in Benard-Marangoni convective structures”. In: *Phys. Rev. E* 54.5 (1996), pp. 5086–5094.

[60] Matthew P. Miklius and Sascha Hilgenfeldt. “Analytical results for size-topology correlations in 2D disk and cellular packings”. In: *Phys. Rev. Lett.* 108 (2012), p. 015502.

[61] N Rivier, D Weaire, and R Romer. “Tetrahedrally Bonded Random Networks Without Odd Rings”. In: *J. Non. Cryst. Solids* 105 (1988), pp. 287–291.

[62] F. T. Lewis. “The correlation between cell division and the shapes and sizes of prismatic cell in the epidermis of cucumis”. In: *Anat. Rec.* 38.3 (1928), pp. 341–376.

[63] M. A. Fortes. “Applicability of the Lewis and Aboav-Weaire laws to 2D and 3D cellular structures based on Poisson partitions”. In: *J. Phys. A* 28 (1995), pp. 1055–1068.

[64] Sangwoo Kim, Muyun Cai, and Sascha Hilgenfeldt. “Lewis’ law revisited: the role of anisotropy in size-topology correlations”. In: *New J. Phys.* 16 (2014), p. 015024.

[65] S. N. Chiu. “Aboav-Weaire’s and Lewis’ laws - A review”. In: *Mater. Charact.* 34 (1995), pp. 149–165.

[66] Renaud Delannay and Gérard Le Caër. “Topological characteristics of 2D cellular structures generated by fragmentation”. In: *Phys. Rev. Lett.* 73.11 (1994), pp. 1553–1556.

[67] S Le Roux and F Rezai-Aria. “Topological and metric properties of microscopic crack patterns : application to thermal fatigue of high temperature”. In: *J. Phys. D* 46 (2013), p. 295301.

[68] David A Noever. “Statistics of emulsion lattices”. In: *Colloids and Surfaces* 62 (1992), pp. 243–247.

[69] J. C. M. Mombach, R. M. C. de Almeida, and J. R. Iglesias. “Two-cell correlations in biological tissues”. In: *Phys. Rev. E* 47.5 (1993), pp. 3712–3717.

[70] P Pedro et al. “Polygonal terrains on Mars : A contribution to their geometric and topological characterization”. In: *Planet. Space Sci.* 56 (2008), pp. 1919–1924.

[71] David P Landau and Kurt Binder. *A Guide to Monte Carlo Simulations in Statistical Physics*. 4th ed. Cambridge University Press, 2014.

[72] David J Wales and Harold A Scheraga. "Global Optimization of Clusters, Crystals, and Biomolecules". In: *Science (80-.).* 285 (1999), pp. 1368–1372.

[73] Andrea C Levi and Miroslav Kotrla. "Theory and simulation of crystal growth". In: *J. Phys. Condens. Matter* 9 (1997), p. 299.

[74] C Ratsch and J A Venables. "Nucleation Theory and the Early Stages of Thin Film Growth". In: *J. Vac. Sci. Technol. A* 21 (2003), S96.

[75] Wlater Kob. "Computer simulations of supercooled liquids and glasses". In: *J. Phys. Condens. Matter* 11 (1999), R85.

[76] Pablo Jensen. "Growth of nanostructures by cluster deposition: Experiments and simple models". In: *Rev. Mod. Phys.* 71.5 (1999), pp. 1695–1735.

[77] Daan Frenkel and Berend Smit. *Understanding Molecular Simulation: from Algorithms to Applications*. 2nd ed. Academic Press, 2002.

[78] M P Allen and D J Tildesley. *Computer simulation of liquids*. 2nd ed. Oxford Science Publications, 2017.

[79] Steve Brooks et al. *Handbook of Markov Chain Monte Carlo*. CRC Press, 2011.

[80] N Metropolis et al. "Equation of State Calculations by Fast Computing Machines". In: *J. Chem. Phys.* 21.6 (1953), pp. 1087–1092.

[81] Vasilios I Manousiouthakis and Michael W Deem. "Strict detailed balance is unnecessary in Monte Carlo simulation". In: *J. Chem. Phys.* 110 (1999), p. 2753.

[82] Hidemaro Suwa and Synge Todo. "Markov Chain Monte Carlo Method without Detailed Balance". In: *Phys. Rev. Lett.* 105 (2010), p. 120603.

[83] Manon Michel, Sebastian C Kapfer, and Werner Krauth. "Generalized event-chain Monte Carlo:" in: *J. Chem. Phys.* 140 (2014), p. 054116.

[84] G M Torrie and J P Valleau. "Nonphysical Sampling Distributions in Monte Carlo Free-Energy Estimation: Umbrella Sampling". In: *J. Comput. Phys.* 23 (1977), pp. 187–199.

[85] David J Earl and Michael W Deem. "Parallel tempering: Theory, applications, and new perspectives". In: *Phys. Chem. Chem. Phys.* 7 (2005), pp. 3910–3916.

[86] Bernd Hartke. "Global Geometry Optimization of Clusters Using Genetic Algorithms". In: *J. Phys. Chem.* 97 (1993), pp. 9973–9976.

[87] J A Niesse and Howard R Mayne. "Global geometry optimization of atomic clusters using a modified genetic algorithm in space-fixed coordinates". In: *J. Chem. Phys.* 105 (1996), p. 4700.

[88] David J Wales and Jonathan P K Doye. "Global Optimization by Basin-Hopping and the Lowest Energy Structures of Lennard-Jones Clusters Containing up to 110 Atoms". In: *J. Phys. Chem. A* 101 (1997), pp. 5111–5116.

[89] S . Kirkpatrick, C . D . Gelatt Jr., and M . P . Vecchi. "Optimization by Simulated Annealing". In: *Science (80-.).* 220.4598 (1983), pp. 671–680.

[90] Darrall Henderson, Sheldon H Jacobson, and Alan W Johnson. “The Theory and Practice of Simulated Annealing”. In: *Handb. Metaheuristics*. Ed. by Fred Glover and Gary A Kochenberger. Boston, MA: Springer US, 2003, pp. 287–319.

[91] F Wooten, K Winer, and D Weaire. “Computer Generation of Structural Models of Amorphous Si and Ge”. In: *Phys. Rev. Lett.* 54.13 (1985), pp. 1392–1395.

[92] M M J Treacy and K B Borisenko. “The Local Structure of Amorphous Silicon”. In: *Science (80-.).* 335 (2012), pp. 950–953.

[93] Yuhai Tu et al. “Properties of a Continuous-Random-Network Model for Amorphous Systems”. In: *Phys. Rev. Lett.* 81.22 (1998), pp. 4899–4902.

[94] B R Djordjevic, M F Thorpe, and F Wooten. “Computer model of tetrahedral amorphous diamond”. In: *Phys. Rev. B* 52.8 (1995), pp. 5685–5690.

[95] Normand Mousseau and G T Barkema. “Binary continuous random networks”. In: *J. Phys. Condens. Matter* 16 (2004), S5183–S5190. arXiv: `0408705 [cond-mat]`.

[96] E M Huisman, C Storm, and G T Barkema. “Monte Carlo study of multiply crosslinked semiflexible polymer networks”. In: *Phys. Rev. E* 78 (2008), p. 051801.

[97] C P Broedersz and F C Mackintosh. “Modeling semiflexible polymer networks”. In: *Rev. Mod. Phys.* 86 (2014), pp. 995–1036.

[98] Sandeep K Jain and Gerard T Barkema. “Rupture of amorphous graphene via void formation”. In: *PCCP* 20 (2018), pp. 16966–16972.

[99] Avishek Kumar, Mark Wilson, and M F Thorpe. “Amorphous graphene: a realization of Zachariasen’s glass”. In: *J. Phys. Condens. Matter* 24 (2012), p. 485003.

[100] P. N. Keating. “Effect of invariance requirements on the elastic strain energy of crystals with application to the diamond structure”. In: *Phys. Rev.* 145.2 (1966), pp. 637–645.

[101] G. Barkema and Normand Mousseau. “High-quality continuous random networks”. In: *Phys. Rev. B* 62.8 (2000), pp. 4985–4990.

[102] D A Drabold. “Topics in the theory of amorphous materials”. In: *Eur Phys J B* 68 (2009), pp. 1–21.

[103] S. von Alfthan, A. Kuronen, and K. Kaski. “Realistic models of amorphous silica: A comparative study of different potentials”. In: *Phys. Rev. B* 68 (2003), p. 073203.

[104] Monica Bulacu et al. “Improved Angle Potentials for Coarse-Grained Molecular Dynamics Simulations”. In: *J. Chem. Theory Comput.* 9 (2013), pp. 3282–3292.

[105] Jorge Nocedal and Stephen J Wright. *Numerical Optimization*. 2nd ed. Springer, 2006.

[106] Normand Mousseau and G. T. Barkema. “Fast bond-transposition algorithms for generating covalent amorphous structures”. In: *Curr. Opin. Solid State Mater. Sci.* 5 (2001), pp. 497–502.

[107] Masaharu Isobe. “Hard sphere simulation in statistical physics - methodologies and applications”. In: *Mol. Simul.* 42.16 (2016), pp. 1317–1329.

[108] Etienne P Bernard, Werner Krauth, and David B Wilson. "Event-chain Monte Carlo algorithms for hard-sphere systems". In: *Phys. Rev. E* 80 (2009), p. 056704.

[109] Joshua A Anderson et al. "Massively parallel Monte Carlo for many-particle simulations on GPUs". In: *J. Comput. Phys.* 254 (2013), pp. 27–38.

[110] Masaharu Isobe and Werner Krauth. "Hard-sphere melting and crystallization with event-chain Monte Carlo". In: *J. Chem. Phys.* 143 (2015), p. 084509.

[111] B Widom. "Random Sequential Addition of Hard Spheres to a Volume". In: *J Chem Phys* 44 (1966), p. 3888.

[112] T S Grigera and G Parisi. "Fast Monte Carlo algorithm for supercooled soft spheres". In: *Phys. Rev. E* 63 (2001), 045102(R).

[113] Andrea Ninarello, Ludovic Berthier, and Daniele Coslovich. "Models and Algorithms for the Next Generation of Glass Transition Studies". In: *Phys. Rev. X* 7 (2017), p. 021039.

[114] A Okabe, B Boots, and K Sugihara. *Spatial Tessellations: Concepts and Applications of Voronoi Diagrams*. Wiley, 1992.

[115] Anne Poupon. "Voronoi and Voronoi-related tessellations in studies of protein structure and interaction". In: *Curr. Opin. Struct. Biol.* 14 (2004), pp. 233–241.

[116] B. J. Gellatly and J. L. Finney. "Characterisation of Models of Multicomponent Amorphous Metals: the Radical Alternative to the Voronoi Polyhedron". In: *J. Non. Cryst. Solids* 50 (1982), pp. 313–329.

[117] FM Richards. "The Interpretation of Protein Structures : Total Volume, Group Volume Distributions and Packing Density". In: *J Mol Biol* 82 (1974), pp. 1–14.

[118] B N Boots. "The Spatial Arrangement of Random Voronoi Polygons". In: *Comput. Geosci.* 9.3 (1983), pp. 351–365.

[119] Masaharu Tanemura. "Statistical Distributions of Poisson Voronoi Cells in Two and Three Dimensions". In: *Forma* 18 (2003), pp. 221–247.

[120] D. Löffler et al. "Growth and structure of crystalline silica sheet on Ru(0001)". In: *Phys. Rev. Lett.* 105 (2010), p. 146104.

[121] Leonid Lichtenstein, Markus Heyde, and Hans Joachim Freund. "Crystalline-vitreous interface in two dimensional silica". In: *Phys. Rev. Lett.* 109 (2012), p. 106101.

[122] Mahdi Sadjadi et al. "Refining glass structure in two dimensions". In: *Phys. Rev. B* 96 (2017), 201405(R).

[123] James F. Shackelford. "Triangle rafts - extended Zachariasen schematics for structure modeling". In: *J. Non. Cryst. Solids* 49 (1982), pp. 19–28.

[124] Christin Büchner et al. "Building block analysis of 2D amorphous networks reveals medium range correlation". In: *J. Non. Cryst. Solids* 435 (2016), pp. 40–47.

[125] Louis Theran et al. "Anchored boundary conditions for locally isostatic networks". In: *Phys. Rev. E* 92 (2015), p. 053306.

[126] P. Tangney and S. Scandolo. "An ab initio parametrized interatomic force field for silica". In: *J. Chem. Phys.* 117 (2002), pp. 8898–8904.

[127] I. Zsoldos and A. Szasz. “Appearance of collectivity in two-dimensional cellular structures”. In: *Comput. Mater. Sci.* 15 (1999), pp. 441–448.

[128] Mahdi Sadjadi and M. F. Thorpe. “Ring correlations in random networks”. In: *Phys. Rev. E* 94 (2016), p. 062304.

[129] S R Broadbent and J M Hammersley. “Percolation processes I. Crystals and Mazes”. In: *Proc. Camb. Phil. Soc.Phil. Soc.* 53 (1956), pp. 629–641.

[130] Duncan S Callaway et al. “Network Robustness and Fragility : Percolation on Random Graphs”. In: *Phys. Rev. Lett.* 85.25 (2000), p. 5468.

[131] Dietrich Stauffer and Amnon Aharony. *Introduction to percolation theory.* 2nd ed. 2014.

[132] M F Sykes and J W Essam. “Exact Critical Percolation Probabilities for Site and Bond Problems in Two Dimensions”. In: *J. Math. Phys.* 5.8 (1964), p. 1117.

[133] Scott Kirkpatrick. “Percolation and Conduction”. In: *Rev. Mod. Phys.* 45.4 (1973), p. 574.

[134] H L Frisch, J M Hammersley, and D J A Welsh. “Monte Carlo Estimates of Percolation Probabilities for Various Lattices”. In: *Phys. Rev.* 126.3 (1962), pp. 949–951.

[135] B Y P Dean and N F Bird. “Monte Carlo estimates of critical percolation probabilities”. In: *Proc. Camb. Phil. Soc.* 63 (1967), p. 477.

[136] M E J Newman. “Mixing patterns in networks”. In: *Phys. Rev. E* 67 (2003), p. 026126.

[137] Di Zhou et al. “Assortativity decreases the robustness of interdependent networks”. In: *Phys. Rev. E* 86 (2012), p. 066103.

[138] C Schmeltzer et al. “Percolation of spatially constrained Erdos-Renyi networks with degree correlations”. In: *Phys. Rev. E* 89 (2014), p. 012116.

[139] V Kapko, D A Drabold, and M F Thorpe. “Electronic structure of a realistic model of amorphous graphene”. In: *Phys. Status Solidi* 247.5 (2010), pp. 1197–1200.

[140] Taishan Zhu and Elif Ertekin. “Phonons, Localization, and Thermal Conductivity of Diamond Nanothreads and Amorphous Graphene”. In: *Nano Lett.* 16 (2016), pp. 4763–4772.

[141] Franz Bamer, Firaz Ebrahem, and Bernd Markert. “Elementary plastic events in a Zachariasen glass under shear and pressure”. In: *Materialia* 9 (2020), p. 100556.

[142] Firaz Ebrahem, Franz Bamer, and Bernd Markert. “Vitreous 2D silica under tension : From brittle to ductile behaviour”. In: *Mater. Sci. Eng. A* 780 (2020), p. 139189.

[143] Oliver Whitaker. “Modelling of complex ring networks in two- and three-dimensions”. PhD thesis. University of Oxford, 2019.

[144] Xiaolei Ma, Janna Lowensohn, and Justin C Burton. “Universal scaling of polygonal desiccation crack patterns”. In: *Phys. Rev. E* 99 (2019), p. 012802.

[145] Hisao Honda. “Description of cellular patterns by Dirichlet domains: The two-dimensional case”. In: *J. Theor. Biol.* 72 (1978), pp. 523–543.

[146] Ross Carter et al. “Pavement cells and the topology puzzle”. In: *Development* 144 (2017), pp. 4386–4397.

[147] Sangwoo Kim et al. “Hexagonal Patterning of the Insect Compound Eye : Facet Area Variatio , Defects, and Disorder”. In: *Biophys. J.* 111 (2016), pp. 2735–2746.

[148] C. J. Lambert and D. L. Weaire. “Theory of the arrangement of cells in a network”. In: *Metallography* 14.4 (1981), pp. 307–318.

[149] Susmit Kumar, Stewart K. Kurtz, and Denis Weaire. “Average number of sides for the neighbours in a Poisson-Voronoi tesselation”. In: *Philos. Mag. B* 69.3 (1994), pp. 431–435.

[150] M. Blanc and A. Mocellin. “Grain coordination in plane sections of polycrystals”. In: *Acta Metall.* 27 (1979), pp. 1231–1237.

[151] N. Rivier. “Statistical crystallography structure of random cellular networks”. In: *Philos. Mag. B* 52.3 (1985), pp. 795–819.

[152] Michael A. Peshkin, Katherine J. Strandburg, and Nicolas Rivier. “Entropic predictions for cellular networks”. In: *Phys. Rev. Lett.* 67.13 (1991), pp. 1803–1806.

[153] S N Chiu. “Mean-Value Formulae for the Neighbourhood of the Typical Cell of a Random Tessellation”. In: *Adv. Appl. Probab.* 26 (1994), pp. 565–576.

[154] J K Mason, R Ehrenborg, and E A Lazar. “A geometric formulation of the law of Aboav – Weaire in two and three dimensions”. In: *J. Phys. A* 45 (2012), p. 065001.

[155] H. J. Hilhorst. “Planar Voronoi cells: The violation of Aboav’s law explained”. In: *J. Phys. A* 39 (2006), pp. 7227–7243.

[156] M. E.J. Newman. “Assortative Mixing in Networks”. In: *Phys. Rev. Lett.* 89.20 (2002), pp. 1–4.

[157] Rogier Noldus and Piet Van Mieghem. “Assortativity in complex networks”. In: *J. Complex Networks* 3 (2015), pp. 507–542.

[158] Alexandros Chremos and Philip J. Camp. “Neighbor network in a polydisperse hard-disk fluid: Degree distribution and assortativity”. In: *Phys. Rev. E* 76 (2007), p. 056108.

[159] Nelly Litvak and Remco van der Hofstad. “Uncovering disassortativity in large scale-free networks”. In: *Phys. Rev. E* 87 (2013), p. 022801.

[160] J M Greneche and J M D Coey. “The topologically-disordered square lattice”. In: *J. Phys. Fr.* 51 (1990), pp. 231–242.

[161] Franz R Eder et al. “A journey from order to disorder - atom by atom transformation from graphene to a 2D carbon glass”. In: *Sci. Rep.* 4 (2014), p. 4060.

[162] Ordnance Survey. *Boundary-Line Data © Crown copyright and database right 2018*. 2018.

[163] Federal Office of Topography. *swissBOUNDARIES3D*. 2019.

[164] Eurostat. *NUTS Geodata © EuroGeographics for the administrative boundaries*. 2016.

[165] Etienne P Bernard and Werner Krauth. "Two-Step Melting in Two Dimensions : First-Order Liquid-Hexatic Transition". In: *Phys. Rev. Lett.* 107 (2011), p. 155704.

[166] Andrew H Marcus and Stuart A Rice. "Phase transitions in a confined quasi-two-dimensional colloid suspension". In: *Phys. Rev. E* 55.1 (1997), p. 637.

[167] Han-Rui Tian et al. "An Unconventional Hydrofullerene C66H4 with Symmetric Heptagons Retrieved in Low-Pressure Combustion". In: *J. Am. Chem. Soc.* 141 (2019), pp. 6651–6657.

[168] Runnan Guan et al. "Stable C92(26) and C92(38) as Well as Unstable C92(50) and C92(23) Isolated-Pentagon-Rule Isomers As Revealed by Chlorination of C92 Fullerene". In: *Inorg. Chem.* 58 (2019), pp. 5393–5396.

[169] Victor A Brotsman, Daria V Ignateva, and Sergey I Troyanov. "Chlorination-promoted Transformation of Isolated Pentagon Rule C78 into Fused-pentagons- and Heptagons-containing Fullerenes". In: *Chem Asian J* 12 (2017), pp. 2379–2382.

[170] Victor A Brotsman et al. "Rebuilding C60 : Chlorination-Promoted Transformations of the Buckminsterfullerene into Pentagon-Fused C60 Derivatives". In: *Inorg. Chem.* 57 (2018), pp. 8325–8331.

[171] Daishi Fujita et al. "Self-assembly of tetravalent Goldberg polyhedra from 144 small components". In: *Nature* 540 (2016), pp. 563–566.

[172] Zhi Wang et al. "Assembly of silver Trigons into a buckyball-like Ag180 nanocage". In: *PNAS* 114.46 (2017), pp. 12132–12137.

[173] A E Roth, C D Jones, and D J Durian. "Coarsening of a two-dimensional foam on a dome". In: *Phys. Rev. E* 86 (2012), p. 021402.

[174] P N Pusey and W Van Megen. "Phase behaviour of concentrated suspensions of nearly hard colloidal spheres". In: *Nature* 320 (1986), p. 340.

[175] Alice L Thorneywork et al. "Radial distribution functions in a two-dimensional binary colloidal hard sphere system". In: *J. Chem. Phys.* 140 (2014), p. 161106.

[176] Alice L Thorneywork et al. "Structure factors in a two-dimensional binary colloidal hard sphere system". In: *Mol. Phys.* 116 (2018), pp. 3245–3257.

[177] R Roth, R Evans, and A A Louis. "Theory of asymmetric nonadditive binary hard-sphere mixtures". In: *Phys. Rev. E* 64 (2001), p. 051202.

[178] R Y Yang, R P Zou, and A B Yu. "Voronoi tessellation of the packing of fine uniform spheres". In: *Phys. Rev. E* 65 (2002), 041302 Voronoi.

[179] VS Kumar and V Kumaran. "Voronoi neighbor statistics of hard-disks and hard-spheres". In: *J Chem Phys* 123 (2005), p. 074502.

[180] A Jaster. "Computer simulations of the two-dimensional melting transition using hard disks". In: *Phys. Rev. E* 59.3 (1999), pp. 2594–2602.

[181] Sander Pronk and Daan Frenkel. "Melting of polydisperse hard disks". In: *Phys. Rev. E* 69 (2004), p. 066123.

[182] Sebastian C Kapfer and Werner Krauth. "Two-Dimensional Melting : From Liquid-Hexatic Coexistence to Continuous Transitions". In: *Phys. Rev. Lett.* 114 (2015), p. 035702.

[183] Alice L Thorneywork. “Structure and dynamics of two-dimensional colloidal hard spheres”. PhD thesis. University of Oxford, 2015.

[184] Matthew O Blunt et al. “Random Tiling and Topological Defects in a Two-Dimensional Molecular Network”. In: *Science (80-.).* 322 (2008), pp. 1077–1081.

[185] P W Anderson. “RESONATING VALENCE BONDS" A NEW KIND OF INSULATOR?” In: *Mat. Res. Bull.* 8 (1973), pp. 153–160.

[186] Philip J Camp, Amparo Fuertes, and J P Attfield. “Subextensive Entropies and Open Order in Perovskite Oxynitrides”. In: *J Am Chem Soc* 134 (2012), pp. 6762–6766.

[187] R Comes, M Lambert, and A Guinier. “THE CHAIN STHUCTURE OF BaT1O3 AND KNbO3”. In: *Solid State Commun.* 6 (1968), pp. 715–719.

[188] G Algara-Siller et al. “Square ice in graphene nanocapillaries”. In: *Nature* 519 (2015), p. 443.

[189] YinBo Zhu, FengChao Wang, and HengAn Wu. “Structural and dynamic characteristics in monolayer square ice”. In: *J. Chem. Phys.* 147 (2017), p. 044706.

[190] Simon J Hibble et al. “Structures of Pd (CN)2 and Pt (CN)2: Intrinsically Nanocrystalline Materials?” In: *Inorg. Chem.* 50 (2011), pp. 104–113.

[191] Qing-Na Zheng et al. “Adaptive Reorganization of 2D Molecular Nanoporous Network Induced by Coadsorbed Guest Molecule”. In: *Langmuir* 30 (2014), pp. 3034–3040.

[192] Lars Postulka et al. “Spin Frustration in an Organic Radical Ion Salt Based on a Kagome-Coupled Chain Structure”. In: *J. Am. Chem. Soc.* 138 (2016), pp. 10738–10741.

[193] Ting Chen et al. “2D Hexagonal Tilings Based on Triangular and Hexagonal Structural Units in the Self-Assembly of Thiacalix[4]arene Tetrasulfonate on an Au(111) Surface”. In: *Chem Asian J* 6 (2011), pp. 1811–1816.

[194] Austin D Griffith and Robert S Hoy. “Densest versus jammed packings of two-dimensional bent-core trimers”. In: *Phys. Rev. E* 98 (2018), p. 042910.

[195] Jose I Urgel et al. “Five-Vertex Lanthanide Coordination on Surfaces: A Route to Sophisticated Nanoarchitectures and Tessellations”. In: *J Phys Chem C* 118 (2014), pp. 12908–12915.

[196] N P Kryuchkov et al. “Complex crystalline structures in a two-dimensional core-softened system”. In: *Soft Matter* 14 (2018), p. 2152.

[197] Bai-Qiao Song et al. “Periodic tiling of triangular and square nanotubes in a cationic metal – organic framework for selective anion exchange †”. In: *Chem Commun* 51 (2015), pp. 9515–9518.

[198] William D Piñeros, Michael Baldea, and Thomas M Truskett. “Designing convex repulsive pair potentials that favor assembly of kagome and snub square lattices”. In: *J. Chem. Phys.* 145 (2016), p. 054901.

[199] Mia Baise et al. “Negative Hydration Expansion in ZrW2O8 : Microscopic Mechanism, Spaghetti Dynamics, and Negative Thermal Expansion”. In: *Phys. Rev. Lett.* 120 (2018), p. 265501.

[200] V A Gorbunov, S S Akimenko, and A V Myshlyavtsev. “Cross-impact of surface and interaction anisotropy in the self-assembly of organic adsorption monolayers : a Monte Carlo”. In: *Phys Chem Chem Phys* 19 (2017), pp. 17111–17120.

[201] Damien Nieckarz, Wojciech Rzysko, and Paweł Szabelski. “On-surface self-assembly of tetratopic molecular building blocks”. In: *Phys Chem Chem Phys* 20 (2018), p. 23363.

[202] C Buzano et al. “Two-dimensional lattice-fluid model with waterlike anomalies”. In: *Phys. Rev. E* 69 (2004), p. 061502.

[203] Philip J Camp. “Structure and phase behavior of a two-dimensional system with core-softened and long-range repulsive interactions”. In: *Phys. Rev. E* 68 (2003), p. 061506.

[204] Michael Griebel and Jan Hamaekers. “Molecular dynamics simulations of boron-nitride nanotubes embedded in amorphous Si-B-N”. In: *Comput. Mater. Sci.* 39 (2007), pp. 502–517.

[205] Arkadiy Simonov et al. “Hidden diversity of vacancy networks in Prussian blue analogues”. In: *Nature* 578 (2020), p. 256.

[206] Marian Florescu, Salvatore Torquato, and Paul J Steinhardt. “Designer disordered materials with large, complete photonic band gaps”. In: *PNAS* 106.49 (2009), pp. 20658–20663.

[207] Steven R Sellers et al. “Local self-uniformity in photonic networks”. In: *Nat. Commun.* 8 (2017), p. 14439.